



# One-pot sol-gel synthesis of MgO nanoparticles supported nickel and iron catalysts for undiluted methane decomposition into CO<sub>x</sub> free hydrogen and nanocarbon



Manoj Pudukudy <sup>a,b,\*</sup>, Zahira Yaakob <sup>a</sup>, Mohd Zulhamizan Mazuki <sup>a</sup>, Mohd Sobri Takriff <sup>b</sup>, Seri Suriani Jahaya <sup>c</sup>

<sup>a</sup> Department of Chemical and Process Engineering, Faculty of Engineering and Built Environment, Universiti Kebangsaan Malaysia, Bangi, 43600, Selangor, Malaysia

<sup>b</sup> Research Center for Sustainable Process Technology (CESPRO), Faculty of Engineering and Built Environment, Universiti Kebangsaan Malaysia, 43600, Bangi, Selangor, Malaysia

<sup>c</sup> Research and Development Centre, Sime Darby Research Sdn. Bhd., Carey Island, 42960 Selangor, Malaysia

## ARTICLE INFO

### Article history:

Received 20 February 2017

Received in revised form 8 April 2017

Accepted 25 April 2017

Available online 26 April 2017

### Keywords:

MgO nanoparticles

Methane cracking

Reaction temperatures

Metal-support interaction

Graphene sheets

## ABSTRACT

A single pot sol-gel method was adopted for the synthesis of MgO nanoparticles supported nickel and iron catalysts for undiluted methane decomposition into CO<sub>x</sub> free hydrogen and nanocarbon for the first time. The catalysts were successfully synthesized via a facile sol-gel route without the assistance of any surfactants. The as-synthesized catalysts were completely characterized for their structural, textural and redox properties using several analytical techniques. The X-Ray diffraction analysis confirmed the formation of NiMgO solid solution and magnesioferrites as the active phases in the fresh catalysts. The inter-aggregation of nanoparticles in the catalyst generated pores, and a mesoporous texture resulted. The hydrogen chemisorption analysis indicated that the NiMgO solid solution was very difficult to reduce compared to the magnesioferrites. The thermocatalytic decomposition of methane at 700 °C, 800 °C and 900 °C fully validated their enhanced catalytic activity and stability for the reaction. The initial hydrogen yield and total carbon yield were found to be significantly increased, when the reaction temperature was increased. However, the highest catalytic performance was shown by the Fe/MgO catalyst. Moreover, no catalyst deactivation was observed for both of the catalysts for a period of 360 min of time on stream. This could be ascribed to their enhanced catalytic stability due to the presence of metal nanoparticles dispersed on the surface of the support, with proper metal-support interaction rather than their specific surface area. Multiwalled carbon nanotubes with metal encapsulated carbon particles and few layered graphene sheets were deposited over Ni/MgO and Fe/MgO catalysts, respectively. The studies of the effect of reaction temperature on the crystalline properties of the deposited nanocarbon indicated that the crystallinity and graphitization degree were increased with increasing reaction temperatures.

© 2017 Elsevier B.V. All rights reserved.

## 1. Introduction

Hydrogen is considered to be a clean and green energy carrier based on its non-emission during combustion. A number of hydrogen production methods are available for the production of energy all over the world. Commonly used hydrogen production methods

include the dry and steam reforming of methane/natural gas, since methane is the abundant source of hydrogen in nature in its free form [1]. Currently, the production of hydrogen by thermocatalytic decomposition of methane is of great interest due to several advantages associated with this process, such as the production of a high concentration of hydrogen, the non-emission of greenhouse gases, low energy consumption and finally the bulk production of highly value-added carbon nanomaterials [2–4]. Because there is no formation of CO<sub>x</sub> in the product gas, the produced hydrogen can be directly applied as an anodic fuel for the proton exchange membrane fuel cells. However, due to the high molecular symmetry of methane, high temperatures were crucial to decompose it, without any catalytic process. In other words, methane decomposition

\* Corresponding author at: Department of Chemical and Process Engineering, Faculty of Engineering and Built Environment, Universiti Kebangsaan Malaysia, Bangi, Selangor 43600, Malaysia.

E-mail addresses: [manojpudukudy@gmail.com](mailto:manojpudukudy@gmail.com), [manojmscp@gmail.com](mailto:manojmscp@gmail.com) (M. Pudukudy).

is an endothermic reaction. Several types of nickel-, cobalt- and iron- based catalysts were effectively reduced the reaction temperatures within a moderate range, under standard experimental conditions [5]. Li et al. [6] previously reviewed that the performance of a catalyst for methane decomposition completely depends on the synthesis methods, nature of the active metal, support, promoter, co-metal, reaction parameters and so on. A number of studies are also available in this regard. The unsupported aforementioned metal catalysts were reported to show low catalytic activity and stability for methane decomposition due to thermal sintering and encapsulation of metal particles at high reaction temperatures. To solve these thermal problems, the utilization of support materials was strategized. It was proved that the presence of support material in the catalyst allows the fine dispersion of active metal on the support, and hence increases the catalytic activity and stability for a prolonged reaction [7]. A number of supported metal catalysts were tested for methane decomposition. Commonly used supports include silica, alumina, magnesia, titania, ceria, zirconia, and lanthana [8]. The metal support interaction is also an important parameter contributing to their catalytic activity and stability [9].

Magnesium oxide is a good material that is, used for a variety of applications, such as catalysts, supports for metals, adsorbents for  $\text{CO}_2$ , photocatalysts for optical activities, agents for antimicrobial activities, and agents for waste water treatment [10–12]. Moreover, it has found a promising role in the field of superconducting and ferroelectric applications [13]. In the catalysis field, it acts as a catalyst or as a catalyst support for many types of organic and inorganic reactions [14]. It has been reported that, compared to other materials,  $\text{MgO}$  nanoparticles serve as excellent support, based on their lower particle size. As the size of the particles decreases, the number of surface atoms increases, and hence the activity is expected to increase [15].  $\text{MgO}$ -supported metal catalysts were already used for a set of catalytic reactions, such as the Fischer-Tropsch reaction, dry and steam reforming of methane, water gas shift reaction and many organic transformations [16–20]. In addition to its existence as a single support material, their mixed oxide with other supports was also used [21]. A number of  $\text{MgO}$  supported metal catalysts were also studied for methane decomposition. However, many of the works were focused on the deposition of nanocarbon from methane.  $\text{MgO}$  is the widely used catalyst support for the growth and deposition of single- and double- walled carbon nanotubes since it allows the formation of highly dispersed metals on the catalyst surface and hence carbon growth [22]. Furthermore,  $\text{MgO}$  can be easily removed from the deposited nanocarbon by normal acid treatments without damaging its structure and crystalline quality [23,24]. Based on these facts,  $\text{MgO}$  has attracted special interest in methane decomposition. A brief description of  $\text{MgO}$ -supported metal catalysts for methane decomposition is presented below. However, only limited studies have focused on hydrogen production.

Awadallah et al. [25] studied  $\text{MgO}$ -supported Ni-Fe, Ni-Co and Fe-Co bimetallic catalysts for methane decomposition into  $\text{CO}_x$  free hydrogen and nanocarbon. They reported that the 25%Fe-25%Co/ $\text{MgO}$  bimetallic catalyst exhibited the highest catalytic activity for a period of 600 min of time on stream with high catalytic stability for hydrogen production. A maximum hydrogen yield of 86% was observed after 270 min on stream for the entire remaining period of reaction. However, the catalytic activities of the Ni-based bimetallic catalysts were found to be low due to the formation of the  $\text{NiMgO}$  solid solution. Borghei et al. [26] reported methane decomposition over Ni-Cu/ $\text{MgO}$  catalyst for the production of pure hydrogen and carbon nanofibres. Torres et al. [27] also produced  $\text{CO}_x$  free hydrogen and carbon nanotubes over Fe-Mo/ $\text{MgO}$  catalyst by methane decomposition. The single-step production of  $\text{CO}_x$  free hydrogen and carbon nanofibres by methane decomposition over Fe and Fe-Mo/ $\text{MgO}$  catalysts was also reported by Pinilla

et al. [28]. According to them, over iron catalysts, approximately 80% methane conversion was achieved, resulting in the deposition of carbon nanofilaments consisting of both chain- like carbon nanofibres and carbon nanotubes. In another work by Pinilla et al. [29], the enhanced catalytic activity of the Ni- and Ni-Cu- loaded  $\text{MgO}$  supported catalysts for methane decomposition was studied. Awadallah et al. [30] again reported the production of hydrogen and carbon nanotubes by methane decomposition over a set of stable  $\text{MgO}$  supported Cr-, Mo- and W- based Co catalysts. Ermakova et al. [31] studied methane decomposition over Cu-doped Ni/ $\text{MgO}$  catalyst and reported lower activity for the Ni/ $\text{MgO}$  catalyst due to the presence of strong metal support interaction developed by the formation of the  $\text{NiMgO}$  solid solution. Ning et al. [32] studied methane decomposition over Fe/ $\text{MgO}$  catalyst prepared by the impregnation method and reported the formation of  $\text{MgFe}_2\text{O}_4/\text{MgO}$  solid solution, when the catalyst was calcined at 950 °C for 8–12 h. They reported that smaller iron particles with the size of less than 5 nm were finely dispersed on the surface of the catalyst, when it was subjected to a thermal treatment with methane. The as-formed iron nanoparticles effectively participated in the decomposition and facilitated the growth and production of single-walled carbon nanotubes. Takenaka et al. [33] studied methane decomposition over a set of supported Ni catalysts and reported that the  $\text{MgO}$  supported nickel catalyst was inactive for the reaction because of the presence of strong metal support interaction, triggered by the formation of the  $\text{NiMgO}$  solid solution. In another work by Takenaka et al. [34],  $\text{MgO}$ ,  $\text{Al}_2\text{O}_3$ ,  $\text{SiO}_2$  and  $\text{TiO}_2$  supported cobalt catalysts were used for catalytic methane decomposition. They reported that  $\text{MgO}$  supported cobalt catalysts exhibited higher catalytic performance due to the presence of the small particle size of cobalt over  $\text{MgO}$ . The cobalt particles with the size of 10–30 nm permitted the growth of carbon nanofibres.

Kang et al. [35] studied methane decomposition over Fe-Mo/ $\text{MgO}$  catalyst for the deposition of single- and double- walled carbon nanotubes. They found that, due to the aggregation of catalyst particles at high reaction temperatures, the amount of deposited double walled carbon nanotubes was increased. Li et al. [36] prepared highly porous  $\text{MgO}$  as a catalyst support for the chemical vapour deposition of methane to produce single walled carbon nanotubes. Jin et al. [37] deposited high quality single walled carbon nanotubes by methane decomposition over Fe/ $\text{MgO}$  catalyst derived from a Feitknecht compound with strong metal-support interaction. Yeoh et al. [38] reported the large-scale production of carbon nanotubes by chemical vapour deposition of methane over  $\text{MgO}$  supported Mo-Co bimetallic catalyst. Wan et al. [39] produced single- and double- walled carbon nanotubes by methane decomposition over Fe/ $\text{MgO}$  catalyst prepared by the direct thermal treatment of metal oxides. Douven et al. [40] produced double-walled carbon nanotubes by the catalytic chemical vapour deposition of methane over Fe-Mo/ $\text{MgO}$  catalyst. Rashidi et al. [41] reported a Co-Mo/ $\text{MgO}$  catalyst for the growth of single walled carbon nanotubes in fixed and fluidized bed reactors by methane chemical vapour deposition. The effect of calcination temperature on the Co-Mo/ $\text{MgO}$  catalyst for the deposition of carbon nanotubes by methane decomposition was also investigated. Yeoh et al. [42] reported that, by increasing the calcination temperature, high carbon yield was obtained with narrow diameter distribution and high graphitization degree, due to the presence of strong metal support interaction. Ago et al. [43] studied methane decomposition over Fe/ $\text{MgO}$  catalyst and reported the effect of metal-support interaction on the growth of single walled carbon nanotubes. They showed that smaller iron particles were produced by the reduction of a precursor oxide with strong metal support interaction. The particle size of the iron effectively controlled the diameter of the deposited single- walled carbon nanotubes. Colomer et al. [44] studied methane decomposition over  $\text{MgO}$  supported Ni, Co and

Fe catalysts for the production of single- walled carbon nanotubes at 1000 °C. Among the catalysts, the Co/MgO catalyst showed good activity.

Govindaraj et al. [45] also reported the growth of carbon nanotubes by methane decomposition over a set of catalysts derived by the reduction of spinel  $Mg_{1-x}M_xAl_2O_4$ , where M = Ni, Co and Fe. According to their results, the iron catalyst provided the highest carbon yield compared to the Ni- and Co- based catalysts. This could be attributed to their proper metal-support interaction in the spinel precursor. Liu et al. [46] used  $Fe_3O_4/MgO$  catalyst for the deposition of single- walled carbon nanotubes by methane decomposition at various reaction temperatures and reported that the as-obtained carbon nanotubes exhibited high graphitization degree. Abdullahi et al. [47] also produced bulk amounts of single- walled carbon nanotubes with narrow chirality and diameter distribution over  $Fe/MgO$  catalyst by methane decomposition. They found that the yield of carbon increased with increasing reaction temperature, while the selectivity towards the formation of single- walled carbon nanotubes was reduced after the optimum temperature due to the dispersion of iron oxide particles in the MgO lattice. They also used the Co/MgO catalyst for the disposition of single walled carbon nanotubes [48]. In another work, Ning et al. [49] reported a lamella-like porous  $Fe/MgO$  catalyst prepared by a hydrothermal method for the growth of double- walled carbon nanotubes with high yield. High quality single- walled carbon nanotubes were produced by methane decomposition over a porous  $Fe/MgO$  catalyst prepared by an ethanol thermal treatment by Nie et al. [50]. Li et al. [51] and Byrne et al. [52] also used MgO supported Pd- and W- doped Cu catalysts for the growth and deposition of bamboo- shaped multiwalled carbon nanotubes. Ago et al. [53] also produced single-walled carbon nanotubes over  $Fe-Mo/MgO$  catalyst by methane decomposition.

Chen et al. [54] used molybdenum modified  $Ni/MgO$  catalysts of the direct decomposition of ethanol for the production of hydrogen- rich gas and multiwalled carbon nanotubes at 600–800 °C. Izadi et al. [55] studied methane decomposition over sol-gel derived nanoporous MgO supported Ni monometallic and Cu-, Co-, and Mo based bimetallic catalysts prepared by an impregnation method. According to their results, maximum carbon and hydrogen yields of 3.62 gC/gNi and 36.16% were obtained over  $Ni/MgO$  catalyst for a period of 60 min of time on stream. The Cu-promoted catalyst showed enhanced catalytic activity and stability with a maximum hydrogen yield of 59% and a carbon yield of 5.85 gC/g Ni. The Mo promotion slightly improved the catalytic activity of the  $Ni/MgO$  catalyst. Yan et al. [56] synthesized  $Ni/MgO$  catalyst by the decomposition of nickel and magnesium nitrate using a dielectric barrier discharge plasma technique and used it for the growth of high- quality carbon nanotubes. Li et al. [57] used Sm modified  $Ni/MgO$  catalysts for methane decomposition to produce multiwalled carbon nanotubes at 650 °C. They reported that the addition of Sm as a promoter improved the catalytic activity and stability of the  $Ni/MgO$  catalyst.

Thus, from the above discussion, it is clear that a number of studies on different catalytic aspects were reported on MgO supported nickel and iron catalysts for methane decomposition, especially for the growth of single- or double- walled carbon nanotubes. Moreover, it is obvious that the overall performance of the catalysts depends on the type and properties of the support material and the method of synthesis. Because the size of the MgO support plays an important role in their catalytic performance, either for the growth of nanocarbon or for the production of hydrogen, a one-pot sol-gel method was adopted here to synthesize the nano-sized nickel- and iron- based monometallic catalysts supported on MgO nanoparticles for the first time. The catalysts were completely characterized for their structural, textural and redox properties. Furthermore, methane decomposition was studied as a catalytic

reaction to investigate their performance in terms of the hydrogen and carbon yield. The effects of reaction temperatures between 700 °C and 900 °C on the catalytic activity, stability and the crystalline properties of the deposited nanocarbon over both of the catalysts were investigated in detail. The nanocarbon deposited was completely characterized to address their structural and crystalline properties by X-Ray diffraction, Field emission scanning and transmission electron microscopy, and Raman spectroscopy. It is worth mentioning that, instead of single-, double- or multiwalled carbon nanotubes, few layered graphene sheets were deposited over the  $Fe/MgO$  catalyst for the first time. To the best of our knowledge, there are no studies yet reported for methane decomposition over one-pot sol-gel derived MgO nanoparticles supported nickel and iron catalysts.

## 2. Experimental

### 2.1. Synthesis of MgO supported Ni and Fe catalysts

All chemicals used in the experiments were of analytical grade and were used as received without further purification. A facile single-pot sol-gel method was employed for the synthesis of MgO supported Ni- and Fe- loaded monometallic catalysts. The amount of Ni and Fe was kept 20 wt.% in the present synthesis. In a typical synthesis, 750 ml of distilled water was mixed with 250 ml of absolute ethanol. To the mixture, the weighed amount of magnesium ethoxide (28.4 g) was slowly added and stirred vigorously for 24 h using a mechanical stirrer to obtain a sol of magnesium oxide, at room temperature. Next, the weighed amount of nitrate precursor of the representative metal (Nickel nitrate hexahydrate for Ni and Iron nitrate nonahydrate for Fe) was dissolved in the minimum amount of distilled water (10 ml) and added to the sol. The sol was again stirred for 4 h after the complete addition of the metal salt solution and kept for ageing at room temperature for 24 h. The as-obtained mixture was then dried slowly at 85 °C in a pre-heated air driven oven. The dried samples were then crushed and ground into fine powder. Finally, the samples were calcined at 700 °C for 5 h to obtain the fresh catalysts. The MgO supported nickel and iron catalysts were named  $Ni/MgO$  and  $Fe/MgO$  respectively. For the characterization of pure MgO, it was also prepared using the same method, but without metal salt addition.

### 2.2. Characterization of fresh and spent catalysts

To determine the actual amount of metal content in the fresh catalysts, the active metallic species were extracted using a hot acid solution of HF, HCl and  $HNO_3$  in 1:1:3 vol ratio at 50 °C for 60 min. Next, the solution was diluted to a pH of 2 with deionized water and analyzed by inductively coupling plasma – optical emission spectroscopy (ICP-OES). The physicochemical characterization of the fresh catalysts were performed by means of powder X-ray diffraction (XRD), Fourier transform infra-red spectroscopy (FTIR), field emission scanning electron microscopy (FESEM) coupled with energy dispersive x-ray spectroscopy (EDX), transmission electron microscopy (TEM), nitrogen adsorption-desorption analysis and temperature programmed reduction (TPR) measurements. The XRD patterns of the fresh and spent catalysts were obtained on a D8 Advance Diffractometer (Bruker) using  $Cu K\alpha$  radiation wavelength of  $\lambda = 1.5406 \text{ \AA}$  with a step size of 0.025° in the angle range of 5–80°. The average crystallite size was calculated based on the Scherrer equation using intense diffraction peaks. The FT-IR spectra of the catalysts were recorded in transmission mode using a thermoscientific NICOLET 6700 IR spectroscope in the region of 400–4000  $\text{cm}^{-1}$  by a direct sampling method. The FESEM images of the as-prepared support, catalysts and the produced nanocar-

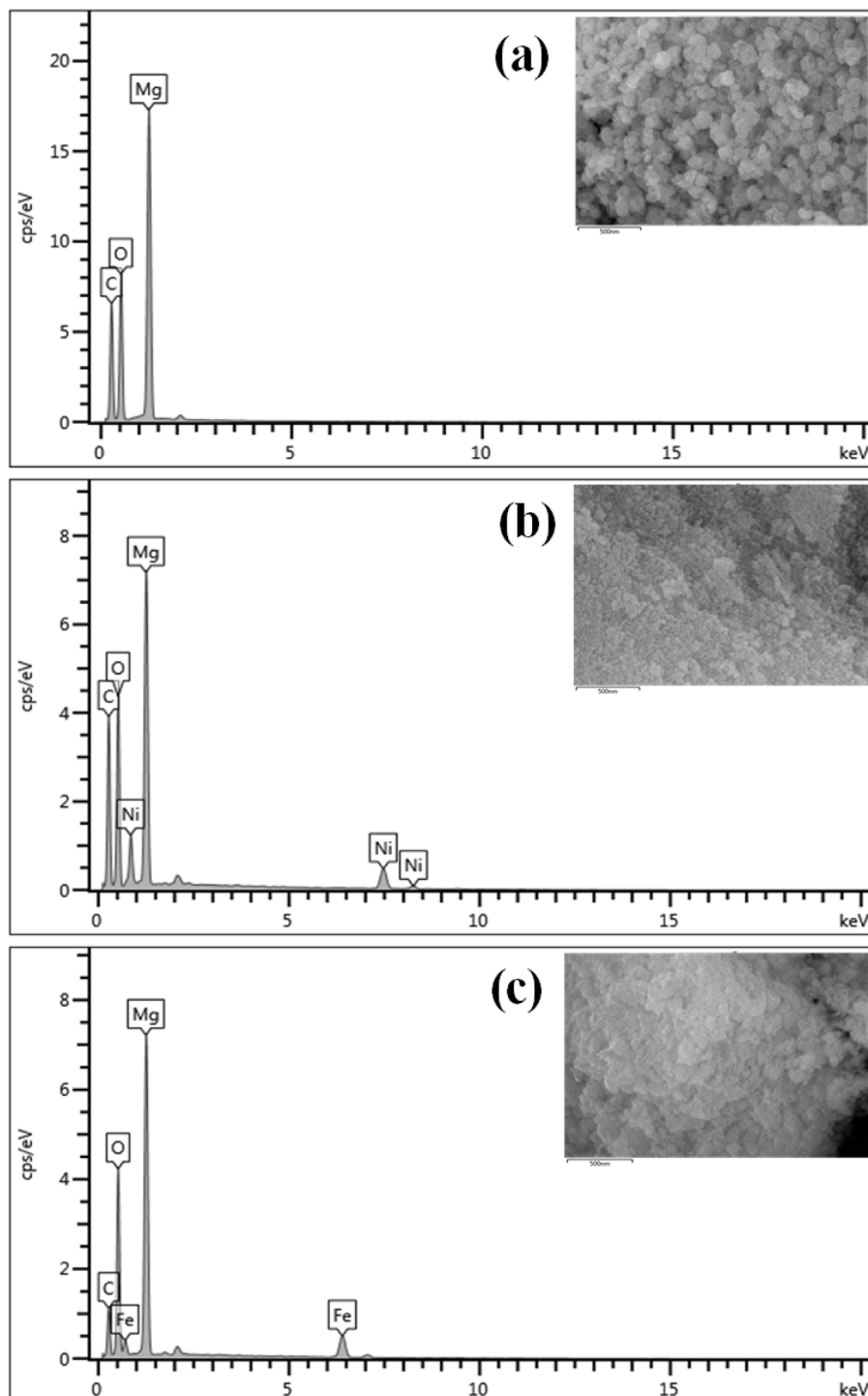


Fig. 1. EDX spectra of the prepared samples (a) support, (b) Ni/MgO and (c) Fe/MgO catalysts.

bon were acquired via a ZEISS MERLIN COMPACT field emission scanning electron microscope, operated at an accelerating voltage of 3 kV. The Energy dispersive X-ray spectroscopy (EDX) system attached to the FESEM microscope was applied to verify the catalyst composition and to determine the metal content on the catalyst surface. The TEM images of the fresh and spent catalysts were acquired using a Philips CM-12 instrument, controlled at an accelerating voltage of 100 kV. The nitrogen sorption experiment such as Brunauer-Emmett-Teller (BET) and Barrett-Joyner-Halenda (BJH) measurements were carried out in a Micromeritics ASAP 2020 apparatus at  $-196^{\circ}\text{C}$ . The samples had previously been degassed at

$300^{\circ}\text{C}$  for 2 h before the analysis. The specific surface area of the catalysts was determined according to the BET method, and the total pore volume was evaluated from the amount of adsorbed  $\text{N}_2$  at a relative pressure of 0.98. The pore diameter distributions were calculated based on the desorption isotherm by the BJH method. The temperature-programmed reduction measurements were used to study the redox behaviour of the catalysts and it was performed in a Micromeritics Autochem 2920 chemisorption analyzer from room temperature to  $800^{\circ}\text{C}$  under a flow of 20 ml/min 20%  $\text{H}_2/\text{N}_2$  gas mixture and a heating rate of  $10^{\circ}\text{C}$  per minute. The hydrogen consumption was monitored by a gas chromatograph equipped with a

thermal conductivity detector (TCD). The crystallinity and graphitization degree of the deposited nanocarbon over the catalysts were studied using Raman spectroscopic analyses. The Raman analysis of the deposited nanocarbon was carried out in a WItec Raman spectrometer (Alpha 300R) equipped with a diode Nd: YAG laser and an excitation wavelength of 532 nm from 10 to 4000  $\text{cm}^{-1}$  [58].

### 2.3. Catalytic activity experiments

The catalytic performance of the as-synthesized catalysts was evaluated for the thermal decomposition of undiluted methane at various temperatures. The experiments were carried out in a vertical tubular up flow cracking reactor made of stainless steel 2520 heated by an electric muffle furnace, as reported in our previous works [8,9,58–60]. The tubular reactor (length of 60 cm, outer diameter of 3.1 cm and inner diameter of 2.5 cm) contains three partitions, and each was coupled with three separate thermocouples. The weighed amount of powder catalyst (1 g) was packed in the middle of the reactor using thermal-resistant quartz wool. Then the catalyst was reduced in situ with a continuous flow of hydrogen (150 ml/min) for 90 min at 700 °C. After reduction, the reactor was flushed with nitrogen to raise the reactor temperature for reaction. The catalytic experiments were carried out at 700 °C, 800 °C and 900 °C under atmospheric pressure (0.1 MPa) using undiluted methane with a flow rate of 150 ml/min for 360 min of time on stream. During the reaction, outlet gas was collected in gas bags at fixed time intervals and were analyzed by a gas chromatograph (SRI GC 8610C) equipped with a Molecular sieve 13X and Porapak Q column connected to a thermal conductivity detector (TCD) with helium as the carrier gas. The yield of hydrogen was calculated using the calibrated data to express the catalytic activity. Hydrogen yield is given by the expression: Hydrogen yield (%) = (Hydrogen (out) / 2 \* (Methane reacted (in))) \* 100. No gases other than hydrogen and unreacted methane were detected in the reaction products. After reaction, the reactor was cooled down to room temperature under a constant flow of nitrogen (50 ml/min), for the collection of carbon-deposited catalysts. The carbon yield was calculated based on the equation reported by Maneerung et al. [61]. Carbon yield (%) = (Weight of carbon deposited on the catalyst / Weight of metal content in the fresh catalyst) \* 100.

## 3. Results and discussion

### 3.1. Catalyst characterization

The quantitative and qualitative characterization of the freshly prepared support and nickel- and iron-loaded MgO catalysts were studied using EDX analysis and the spectra are shown in Fig. 1. As shown in Fig. 1(a), only Mg and O were detected as the main elements in the support, indicating the formation of pure MgO, without any other elemental impurities. In addition to Mg and O, both nickel and iron were detected in the Ni- and Fe-loaded MgO catalysts as shown in Fig. 1(b, c). This suggests that the active metals, such as Ni and Fe, were successfully loaded into the MgO support. The quantitative reports demonstrate the actual amount of Ni and Fe in the fresh catalysts, which were measured to be 16.3 wt% and 16.9 wt%, respectively, in the representative catalysts. This is quite close to the nominated metal content in the fresh catalysts. The peak for carbon in Fig. 1 was originated from the carbon tape used for the sample preparation in SEM-EDX analysis. The chemical composition of the prepared metal catalysts was further studied using ICP-OES analysis, and the results are tabulated in Table 1. As seen, the Ni/MgO and Fe/MgO catalysts show a total metal content of 12.6 wt% and 17.2 wt% for nickel and iron respectively. The actual amount of nickel was quite lower than the nominated metal con-

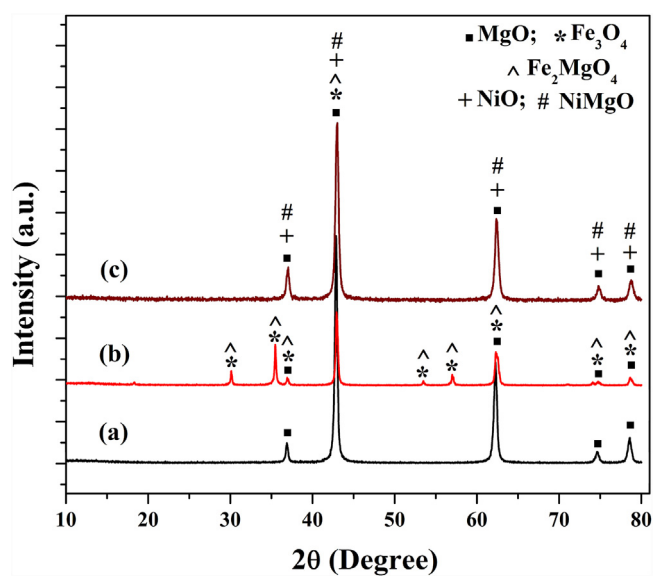


Fig. 2. X-Ray diffraction patterns of the prepared samples (a) support, (b) Fe/MgO and (c) Ni/MgO.

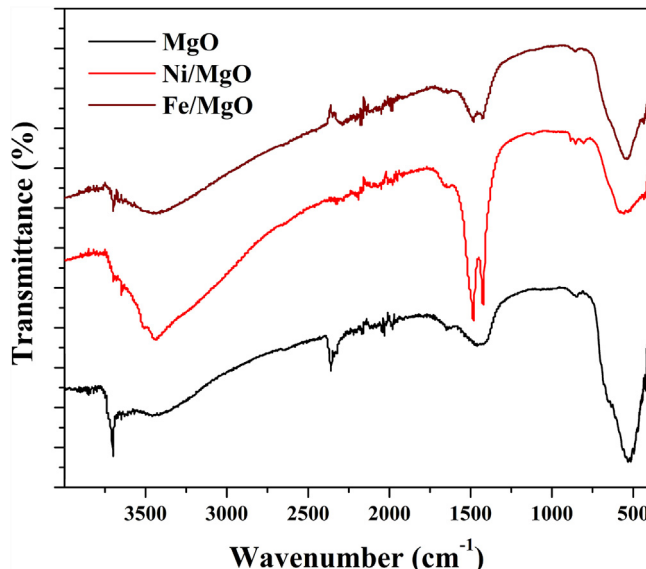
tent in the Ni/MgO catalyst, whereas only minimal variation was observed for the nominated and actual metal content in the Fe/MgO catalyst. The lower metal content detected for the Ni/MgO catalyst could be attributed to the incomplete dissolution of the metallic species in hot acidic solution, due to the strong metal-support interaction.

The crystalline structure and phase purity of the as-prepared support and catalysts were studied using XRD analysis, and the diffraction patterns are shown in Fig. 2. The diffraction peaks centered at the 2θ values of 36.89°, 43°, 62.30°, 74.71° and 78.63° as shown in Fig. 2(a) were directly indexed to the formation face centered cubic phase crystalline structure of MgO with a lattice constant of 0.42112 nm (JCPDS pattern: 00-045-0946). Some other diffraction peaks were identified in the Fe/MgO sample as shown in Fig. 2(b). The diffraction peaks observed at the 2θ values of 36.06°, 35.45°, 36.89°, 42.86°, 53.52°, 56.94°, 62.33°, 74.85° and 78.54° could be attributed to the formation of the face-centered cubic phase crystalline structure of magnesioferrites ( $\text{Fe}_2\text{MgO}_4$ ) with the lattice parameter of 0.8393 nm (JCPDS pattern: 01-077-8656). These peaks were also related to the existence of the face-centered cubic phase of  $\text{Fe}_3\text{O}_4$  (JCPDS pattern: 01-086-1344). However, in the case of the Ni/MgO sample, as in Fig. 2(c), the diffraction peaks were directly indexed to the face-centered cubic phase crystalline structure of the NiMgO solid solution with a lattice constant of 0.4192 nm (JCPDS pattern: 00-045-0946). These peak positions were also similar to those of MgO and NiO. However, it was very hard to make a distinction between them, in such a mixed composition. It is well known that the introduction of an active metal like nickel into the MgO lattice could facilitate the formation of a solid solution [62]. The high intensity of the diffraction peaks suggests that all of the samples were highly crystallized. The peak intensities of the metal loaded catalysts were found to deviate from that of the pure MgO support. After loading with iron, the peak intensities of the catalyst were decreased, suggesting the reduced crystallinity of the Fe/MgO catalyst. However, a reverse trend was observed for the Ni/MgO catalyst. The crystallinity of the Ni/MgO catalyst was quite higher than that of the MgO support. This could be attributed to the formation of a perfect NiMgO solid solution. It was also clear that the magnesioferrites are weakly crystallized compared to the NiMgO solid solution. Moreover, the fine dispersion of metal oxides on the catalyst surface was expected to decrease the crystallinity

**Table 1**

Chemical composition and BET/BJH properties of the fresh catalysts.

Catalyst	Total metal content (wt.%)		Crystalline size (nm)	Surface area (m <sup>2</sup> /g)	Mean pore size (nm)	Pore volume (cm <sup>3</sup> /g)
	Nominated	<sup>c</sup> Actual				
MgO	–	–	23.8	38.60	16	0.1861
Ni/MgO	20	<sup>a</sup> 12.6	<sup>b</sup> 16.3	24.20	18	0.1263
Fe/MgO	20	<sup>a</sup> 17.2	<sup>b</sup> 16.9	17.99	21	0.0970

<sup>a</sup> ICP-OES.<sup>b</sup> EDX analysis.<sup>c</sup> Measured by two methods.**Fig. 3.** FTIR spectra of the prepared samples.

of the supported catalyst. The crystalline sizes of the as-prepared MgO support and metal loaded catalysts were calculated from the intense reflection peak at the  $2\theta$  value of  $43^\circ$ , using Scherrer's equation and were found to be 23.8 nm, 17.8 nm and 29.9 nm for the MgO, Fe/MgO and Ni/MgO samples, respectively.

FTIR spectroscopy was used to study the surface composition and bonding information of the synthesized samples, and the spectra are shown in Fig. 3. The broad transmission band centered at  $\sim 3440\text{ cm}^{-1}$  was assigned to the O–H stretching vibration, due to the presence of physically adsorbed water molecules. MgO has a great tendency to react with water from air, and it rapidly transformed into  $\text{Mg}(\text{OH})_2$ . The intense transmission band centered at  $\sim 3717\text{ cm}^{-1}$  could be attributed to the A2u(OH) lattice vibration of the as-formed  $\text{Mg}(\text{OH})_2$  [63]. The intense peaks in the region of  $1450\text{ cm}^{-1}$  were ascribed to the bending mode vibration of O–H groups bonded with Mg on different co-ordination sites [64]. The well resolved intense transmission band in the region of  $783\text{--}431\text{ cm}^{-1}$ , centered at  $525\text{ cm}^{-1}$  was attributed to the stretching vibrations of the Mg–O bond [65]. After metal loading, the intensity of the stretching vibration of the Mg–O bond was observed to be weakened. This could be attributed to the strong metal–support interaction of the MgO with metal species. Additionally, the transmission band was found to be quite shifted to higher wavenumbers of  $578\text{ cm}^{-1}$  and  $554\text{ cm}^{-1}$ , which further confirms the formation of NiMgO and  $\text{Fe}_2\text{MgO}_4$  solid solutions. However, the band positions of the metal loaded catalysts were found to be the same as in MgO support, indicating the structural stability of the prepared catalysts.

The surface morphologies of the as-prepared support and the catalysts were studied using FESEM analysis, and images are shown in Figs. 4 and 5. Fig. 4 shows the FESEM images of the MgO support

at different magnifications. As shown in Fig. 4(a), flake-like larger units of MgO was observed in the low magnification images. The sizes of the flakes were found to be varied from 15 to 50 micrometers in several dimensions. Moreover, the surface of the flakes was observed to be highly rough and porous. The high magnified images shown in Fig. 4(c, d) show that the flakes were comprised of a large number of MgO nanoparticles. The nanoparticles were highly homogeneous, hierarchical and observed to be more or less spherical in shape with the average size/diameter of  $22 \pm 2\text{ nm}$ . The MgO nanoparticles were found to be highly inter-aggregated, providing a porous appearance to the material. The nanospherical morphology of MgO is very rarely reported in the literature, since many of the synthesis methods produce MgO nanoflakes [66]. Therefore it is interesting to study the catalytic properties of such MgO nanoparticles.

The surface morphologies of the Ni- and Fe- loaded MgO catalysts are shown in Fig. 5. A similar surface morphology was also observed for the metal- loaded catalysts. However, after metal loading, the nanoparticles appeared to be more tightly aggregated than pure MgO, as shown in Fig. 5(c, f). In the Fe/MgO sample, the particles were twinned each other, and larger particles with irregular size and shape resulted. The TEM images of the Ni and Fe loaded MgO catalysts at two different scales are shown in Fig. 6. As seen, more or less spherically shaped nanoparticles with a size ranging from 20 nm to 25 nm were observed. The Ni/MgO catalyst was found to contain a similar type of nanoparticle and a similar particle arrangement, as shown in Fig. 6(a–b). However, highly aggregated irregular particles were observed in the Fe/MgO catalyst. The inter-aggregation of these nanoparticles in the metal catalysts generated a porous structure. This is highly correlated to the FESEM results. Moreover, no distinction between the metals and MgO were observed, indicating the fine dispersion of active metals on the MgO support. SEM-mapping analysis of the samples was further carried out to study the metal dispersion of the catalysts. As shown in Fig. SD1, only Mg and O were detected in the mapping analysis. The active metals, such as Ni and Fe, were found to be excellently dispersed on the MgO support, as shown in the mapping results in Figs. SD2 and SD3.

The textural properties of the as-prepared samples were studied using nitrogen physisorption analysis, and the BET adsorption desorption isotherms are shown in Fig. 7. The isotherms shown in Fig. 7 belong to type IV with a H3 hysteresis loop. These types of hysteresis loops were developed due to the capillary condensation of nitrogen in the mesopores of the samples. Hence it is a characteristic of the mesoporous materials with slit- like pores. The slit- shaped pores were expected to be generated from the inter-aggregation of nanoparticles. This observation is highly consistent with the FESEM and TEM results. Moreover, it was found that the nitrogen uptake of pure MgO started at a relative pressure of  $(P/P_0)$  0.4, whereas, for the Ni- and Fe- loaded catalysts, the nitrogen uptake started at the relative pressure range of 0.6 and 0.85, respectively. This indicates that the sol-gel- synthesized MgO takes a highly porous structure compared to the metal- loaded MgO catalysts. This is highly consistent with the BET/BJH results

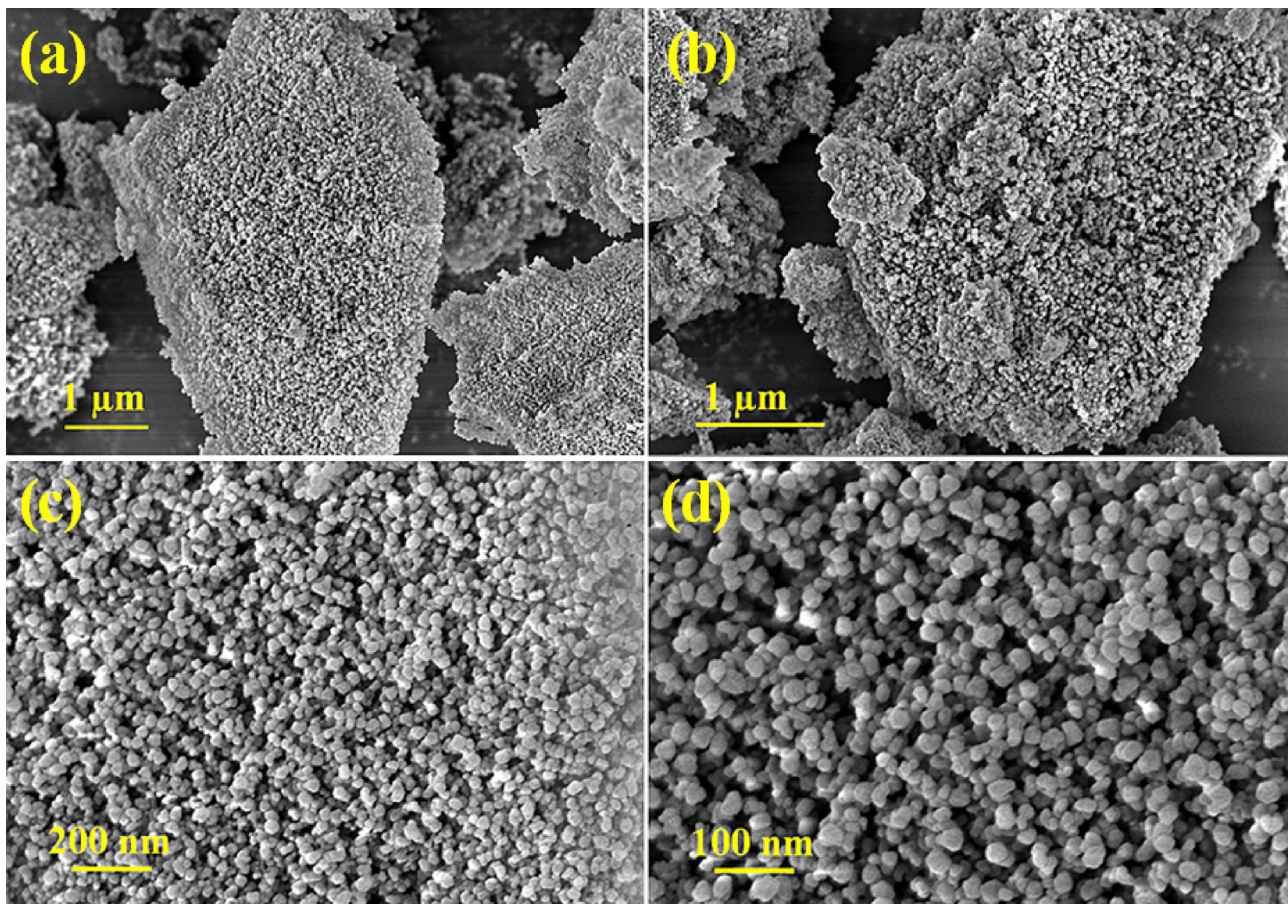


Fig. 4. FESEM images of the sol-gel derived MgO nanoparticles.

shown in Table 1. The BET surface area of the sol-gel derived MgO support was measured to be  $\sim 38.6 \text{ m}^2/\text{g}$  with an average pore size of 16 nm and a pore volume of  $0.1861 \text{ cm}^3/\text{g}$ . After metal loading, the surface area of the MgO catalysts was found to significantly drop. The measured surface area was found to be  $\sim 24.2 \text{ m}^2/\text{g}$  and  $\sim 17.99 \text{ m}^2/\text{g}$  for the Ni/MgO and Fe/MgO catalysts, respectively. The reduced surface area of the catalysts after metal loading could be ascribed to the pore blocking of the MgO support after metal incorporation [67]. Moreover the formation of the solid solution was expected to drop the surface area. For Ni/MgO and Fe/MgO catalysts, the pore size and pore volume were calculated to be 18 nm and  $0.1263 \text{ cm}^3/\text{g}$  and 21 nm and  $0.0970 \text{ cm}^3/\text{g}$ , respectively. The pore volume of the MgO support was decreased after metal loading, in both of the metal loaded catalysts. However, a drastic decrease in pore volume was observed for the iron loaded catalyst. However, the pore size remained almost the same, but slightly increased after metal loading, which could be attributed to the presence of empty spaces in between the larger particles formed by the aggregation of nanoparticles, as explained in the electron microscopic results.

The reduction behaviours of the nickel- and iron- loaded MgO catalysts were studied using hydrogen-temperature programmed reduction analysis, and the reduction profiles are shown in Fig. 8. Both of the catalysts exhibited a wide reduction profile at a high temperature range with several maximas. It was reported that the metal loaded MgO catalysts are very difficult to reduce, especially the NiMgO solution. Parmaliana et al. [68] studied the effect of calcination temperatures ( $400^\circ\text{C}$  to  $1000^\circ\text{C}$ ) on the reduction properties of the Ni/MgO catalysts. According to their results, with increasing calcination temperature, a perfect NiMgO solid solution was formed, which is indicated by the absence of low- tempera-

ture reduction peaks in the TPR profile. Our results also support their assumption. As shown in Fig. 8, a wide reduction profile from  $300^\circ\text{C}$  to  $850^\circ\text{C}$  with several maximas at  $324^\circ\text{C}$ ,  $401^\circ\text{C}$ ,  $454^\circ\text{C}$  and  $742^\circ\text{C}$  was observed for the Ni/MgO catalyst. These reduction peaks were either related to the possible reduction of nickel cations (bi/trivalent) positioned in the lattice of MgO crystal, i.e., the NiMgO solid solution, or due to the reduction of interacting NiO particles dispersed on the surface of the MgO support [69]. However, it is not possible to ensure the complete reduction of the NiMgO solid solution due to the presence of strong metal-support interaction. A broad reduction peak in the temperature range of  $300^\circ\text{C}$  to  $900^\circ\text{C}$  with two well resolved maxima at  $465^\circ\text{C}$  and  $541^\circ\text{C}$  and a shoulder peak at  $694^\circ\text{C}$  were observed for the Fe/MgO catalyst. These peaks were related to the reduction of magnesioferrites. The stepwise reduction of isolated  $\text{Fe}_3\text{O}_4$  cannot be discarded. However, due to the variations in the synthesis methods and the differences in the applied experimental conditions for the TPR analysis, it is hard to assign the reduction peaks of the supported Ni and Fe catalysts as reported by Wurzler et al. [70]. Usually, the low temperature reduction peaks were related to the reduction of metal oxides, which weakly interact with the support material, whereas a high reduction temperature was observed for the reduction of metal oxides with strong metal support interaction [71]. Thus, in the present case quite high reduction temperatures were observed for both of the catalysts, indicating the strong interaction between the active metal and support. It further validates the formation of the NiMgO and  $\text{Fe}_2\text{MgO}_4$  solid solutions.

It is well known that the metal-support interaction has a crucial impact on the reduction of metal oxides and the dispersion of metals on the supported catalysts. The strong metal-support inter-

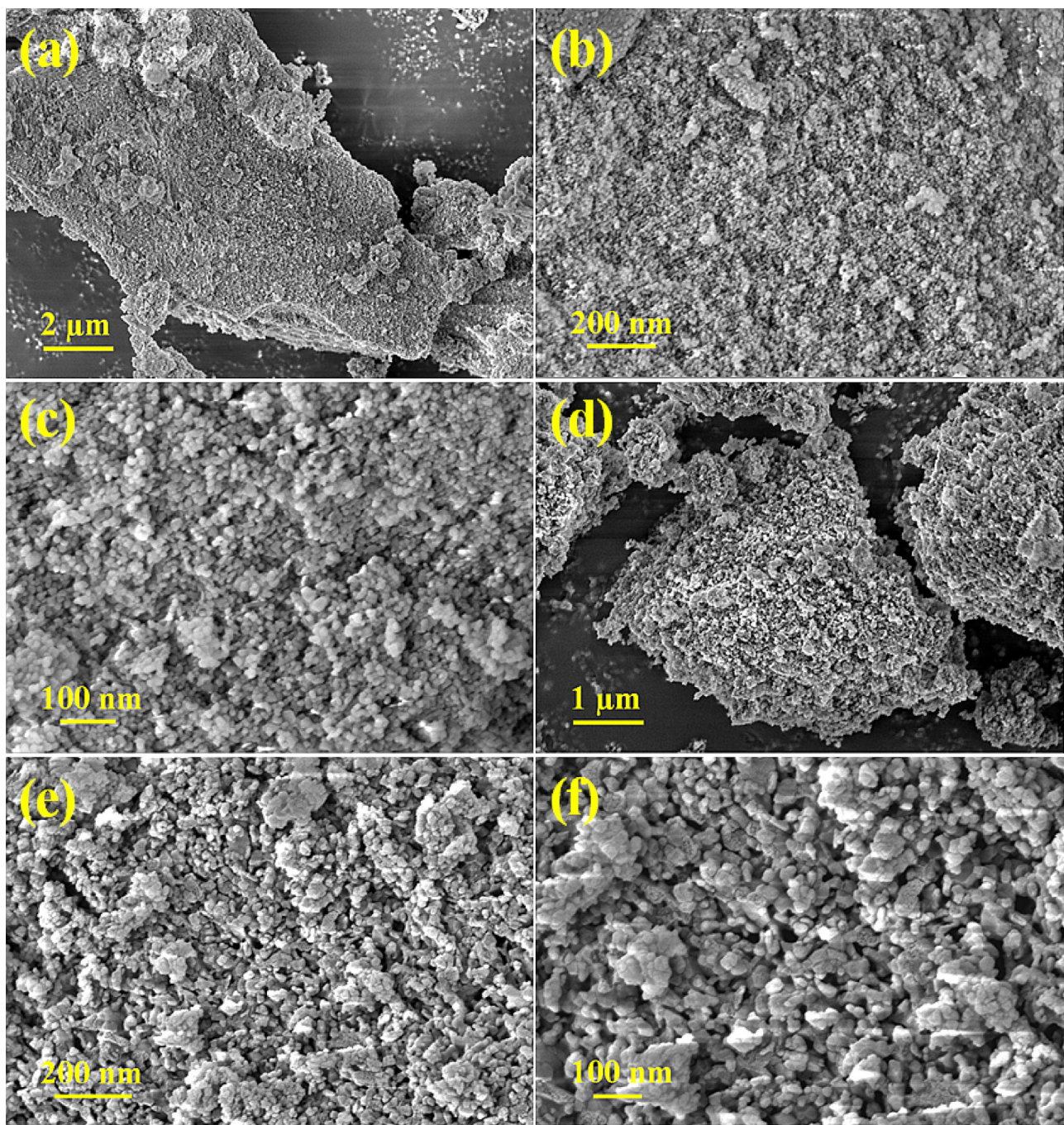


**Fig. 5.** FESEM images of the fresh catalysts at different magnifications (a–c) Ni/MgO and (d–e) Fe/MgO.

action in the catalyst makes the reduction of catalyst precursor oxide very difficult either by increasing the reduction temperatures or by the formation of a metal-support species as reported by Li et al. [6]. Moreover, a strong metal-support interaction decreases the surface mobility of the metal particles, and their metal dispersion could be enhanced. It may affect the electronic and crystallographic states of the metals and hence influence the activity and stability of the catalyst for methane decomposition [6]. Hu et al. [72] reported that the nickel catalyst obtained by the reduction of the NiO-MgO solid solution has a very small particle size and enhances its dispersion on the catalyst surface and hence high catalytic performance was noted. Another work by Gac et al. [73] reconfirmed the production of small nickel crystallites by the reduction of the NiMgO solid solution, and a high initial reaction rate was observed for the

reaction. Therefore, these catalysts were expected to be active and stable for the catalytic methane decomposition [74].

### 3.2. Catalytic performance for methane decomposition

The catalytic performance of the as-prepared catalysts was studied for the thermal decomposition of undiluted methane at various reaction temperatures. The hydrogen yield as a function of time on stream over Ni- and Fe- loaded MgO catalysts at various reaction temperatures is shown in Fig. 9. Only hydrogen and unreacted methane were detected in the product gas, in all of the experiments. Fig. 9(a) shows the kinetic curves of methane decomposition over Ni/MgO catalyst. As shown in Fig. 9(a), the reaction temperatures slightly affected the initial hydrogen yield of the reaction. This could

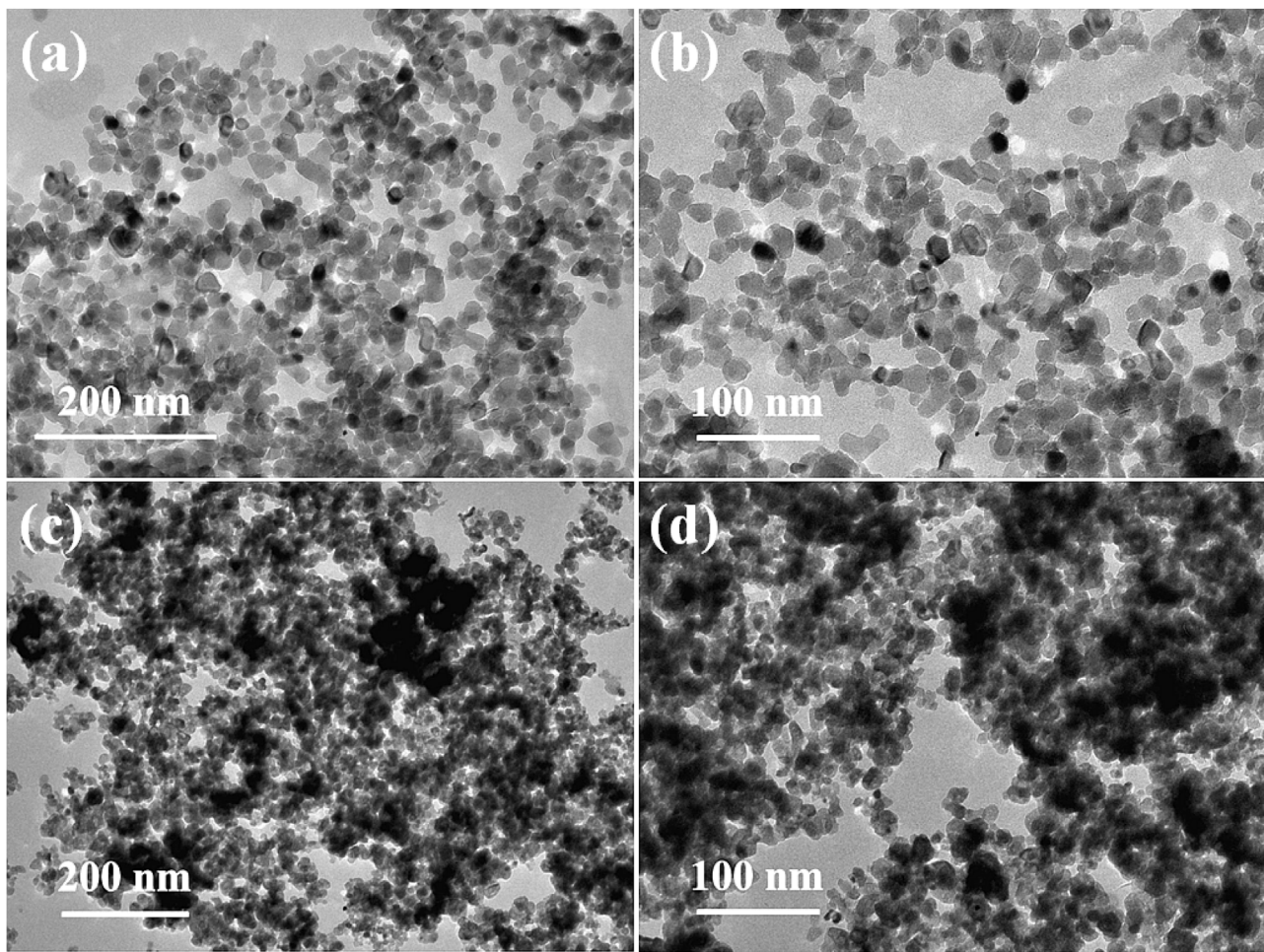


**Fig. 6.** TEM images of the prepared samples (a, b) Ni/MgO and (c, d) Fe/MgO catalysts.

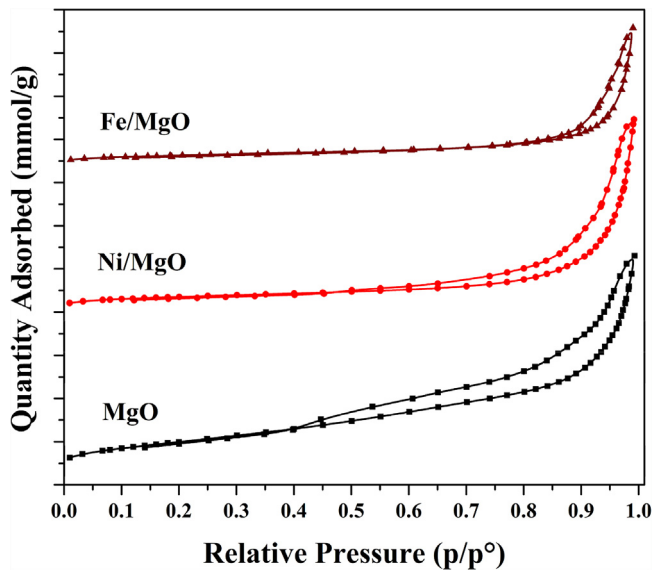


**Fig. 7.** Nitrogen sorption isotherms of the prepared samples.

be due to the endothermic nature of the methane decomposition reaction. After 240 min of time on stream, the yield of hydrogen remained more or less the same at all of the studied reaction temperatures. A maximum hydrogen yield of 43% was obtained for the Ni/MgO catalyst at 700 °C within the first 10 min of time on

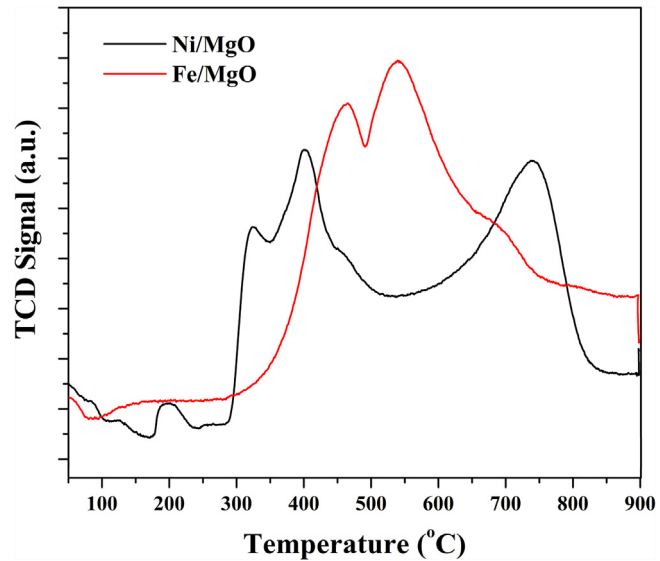


**Fig. 8.** TPR profiles of the freshly prepared catalysts.

stream. After that, a slight decrease of the hydrogen yield to 38% was observed at 30 min of time on stream, and it remained more or less the same ( $35 \pm 2\%$ ) for the entire period of 360 min of reaction. A significant increase in the hydrogen yield was observed for the nickel catalyst, when the reaction temperature was increased

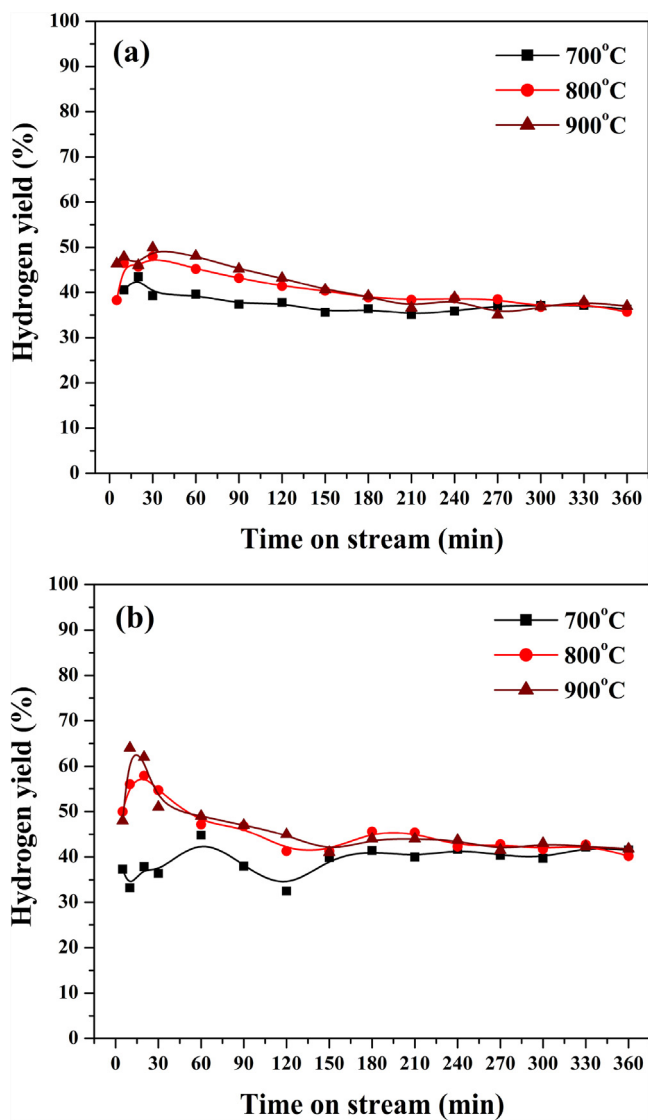


**Fig. 9.** Hydrogen yield as a function of time on stream over (a) Ni/MgO and (b) Fe/MgO catalysts.

to 800 °C. Within the first 30 min of time on stream, the yield of hydrogen increased from 38% to 47%. During the next 120 min of time on stream, the hydrogen yield was observed to slightly decline, and at 180 min of time on stream, ~37% hydrogen yield was noted. After the slight decline the yield of hydrogen remained more or less the same ( $36 \pm 2\%$ ) for the entire 360 min of reaction. Only a small difference in the hydrogen yield was observed for the nickel catalyst when the reaction temperature was further increased to 900 °C. At 900 °C, the initial hydrogen yield was increased from 46% to 51% within the first 30 min of time on stream. After a linear, but slow decrease of the hydrogen yield to 40% at the 180 min of time on stream, it remained almost the same ( $36 \pm 2\%$ ) for the entire remaining period of the decomposition reaction. The yield obtained at 900 °C towards the end of the reaction was found to be somewhat same as the yield obtained at the reaction temperatures of 800 °C and 700 °C. This could be attributed to the strong metal-support interaction of the catalyst, due to the formation of the hardly reducible NiMgO solid solution. The increase in the reaction temperature from 700 °C to 900 °C could not contribute to the complete reduction of the NiMgO solid solution to active metallic species for the reaction, and hence a minimal effect on the initial hydrogen yield was observed. However, the activity and stability

of the Ni/MgO catalyst could be attributed to the effect of strong metal-support interaction. It is expected that the reduction of the NiMgO solid solution produced smaller nickel crystallites, which would effectively contribute to the catalytic activity and stability for methane decomposition, as reported previously [33,72,73].

Fig. 9(b) shows the effect of reaction temperature on methane decomposition as a function of time on stream over Fe/MgO catalyst. A high yield of hydrogen was observed for the Fe/MgO catalyst compared to the Ni/MgO catalyst. As in the nickel catalyst, only unreacted methane and hydrogen were detected in the product gas. At 700 °C, the yield of hydrogen was found to increase from 33% to 45% in the first 60 min of time on stream. After 150 min of reaction, the hydrogen yield remained almost the same ( $41 \pm 1\%$ ) for the entire remaining period of the reaction. With a further increase in the reaction temperature, a significant increase in the initial hydrogen yield was observed, due to the endothermic nature of the reaction. A maximum hydrogen yield of 57% was achieved at 800 °C within the first 20 min of reaction. After a slight decline to 42%, the catalyst exhibited a stable performance for the next whole duration of reaction. The yield of hydrogen remained more or less the same, i.e.,  $42 \pm 2\%$  for the entire period of reaction. At a reaction temperature of 900 °C, the yield of hydrogen was increased from 48.5% to 64% in the first 10 min of reaction, and it remained almost unchanged in the next 10 min of reaction. After that, the hydrogen yield started to decrease, and a 50% yield was observed at the end of 60 min of time on stream. After a gradual decrease of the hydrogen yield to 42%, it remained as such for the entire remaining period of the reaction. It can also be noticed that the yield of hydrogen at 800 °C and 900 °C over Fe/MgO catalyst was almost the same after the first 60 min of the reaction. As explained before, the high catalytic activity and stability of the catalysts for methane decomposition could be due to the formation of nanosized iron particles by the reduction of magnesioferrites having strong metal-support interaction.

Table 2 shows a comparison of the activities of the Ni/MgO and Fe/MgO catalysts for hydrogen production at all of the reaction temperatures. The final hydrogen yield at the end of 360 min of time on stream was found to be the same, i.e.,  $\sim 37\%$  and  $\sim 42\%$ , for the Ni/MgO and Fe/MgO catalysts respectively at 700 °C, 800 °C and 900 °C. The initial activity of the Fe/MgO catalyst was found to be drastically increased when the reaction temperature was increased from 700 °C to 900 °C. However, a drastic increase was not observed for the Ni/MgO catalyst. This indicates the high catalytic activity of the Fe/MgO catalyst in the initial stage of reaction. Moreover, the difference between the highest initial and final hydrogen yield shows that the Ni/MgO catalyst exhibited a small yield difference compared to the Fe/MgO catalyst at the representative temperatures, which points to the fact that Ni/MgO is more stable than the Fe/MgO catalyst; even it exhibited a stable performance after a highest initial performance for decomposition. The decreased hydrogen yield with increasing time on stream could be attributed to the surface coverage of nanocarbon on the catalyst particles. It possibly reduces the availability of the active sites for methane molecules to participate in the catalytic decomposition. The variations in the performance of the Ni/MgO and Fe/MgO catalysts could be more related to their metal-support interaction than the specific surface area. The surface area is not a prominent factor, played over these catalysts since the highest surface area was shown by the Ni/MgO catalyst compared to the Fe/MgO catalyst. However, the highest catalytic activity was shown by the Fe/MgO catalyst at all of the studied reaction temperatures. This points to the enhanced role of metal-support interaction for the reaction. The relative low activity of the Ni/MgO catalyst could be ascribed to the difficulty in the reduction of the NiMgO solid solution compared to magnesioferrites. The XRD analyses of the spent catalysts at various reaction temperatures were used to explain this fact more clearly.

**Table 2**

Activity and stability of the catalysts in terms of hydrogen yield at various reaction temperatures.

Reaction Temperature(°C)	Hydrogen yield over Ni/MgO catalyst (%)			Hydrogen yield over Fe/MgO catalyst (%)		
	Highest	Initial	Final	Difference	Highest	Initial
700	43	36	36	7	45	41
800	47	37	37	10	57	42
900	51	37	37	14	64	42

In the literature, only a few studies have been reported for hydrogen production by methane decomposition over MgO supported catalysts, as discussed in the introduction [25–34,55]. However, a comparison of the catalytic performance of the current catalysts with some of the recently reported catalysts is discussed briefly. Kang and Lee [75] studied methane decomposition over nickel–carbon–B<sub>2</sub>O<sub>3</sub> core–shell structured catalysts synthesized by a one-step chemical method using carbon dioxide, sodium borohydride and nickel carbonate as the precursors at 500 °C and 1 bar. A maximum methane conversion of ~90% was obtained over the 13%Ni@C–B<sub>2</sub>O<sub>3</sub> catalyst at 850 °C with a methane space velocity of 46.15 l/hgNi. It showed high catalytic stability for 15 cycles of reaction, after regeneration by each run. According to them, the activity and stability of the catalyst was due to its core shell structure. More clearly, during the generation of carbon nanonions, the nickel encapsulated by the deposited carbon was easily migrated through the amorphous carbon shell, before being deactivated, and the migrated nickel particle was then re-used to produce hydrogen and new carbon nanonions. Tang et al. [76] studied methane decomposition over ceria modified iron catalysts prepared by a co-precipitation method. They reported that the Fe/CeO<sub>2</sub> catalyst showed better catalytic activity than the bare iron catalyst, due to the fine dispersion of iron on the ceria support. However, the 60%Fe/CeO<sub>2</sub> catalyst exhibited the highest iron surface area among the prepared catalysts, and it yielded a maximum methane conversion of ~80% in the initial stage of reaction. The catalyst was found to be stable for 720 min of time on stream, with a steady state methane conversion of 23% at 750 °C with a catalyst dose of 150 mg and a methane flow rate of 10 ml/min with 30% methane in argon. Bayat et al. [77] recently used sol-gel made alumina as a catalyst support for Ni–Cu catalysts and studied their potential application for methane decomposition. According to their results, a maximum methane conversion of ~84% was observed in the initial stage of the reaction over 50%Ni–10%Cu/Al<sub>2</sub>O<sub>3</sub> catalyst at 750 °C, and it showed a gradual decrease with increasing time on stream. However, a steady state methane conversion of 70% was observed at 675 °C for a period of 700 min of time on stream. Wang and Lua [78] used Ni–Cu alloy nanoparticles prepared by the thermal decomposition of NiCu oxalates for methane decomposition. According to their results, the Ni–Cu alloy catalyst with 62.5% Ni showed a maximum methane conversion of ~82% at 750 °C. The catalysts showed high catalytic stability for a period of 400 min of time on stream. In another work, Naresh et al. [79] used nanosized H $\beta$  zeolite supported Ni and Ni–Cu catalysts prepared by an impregnation method for methane decomposition. They reported that NiCu alloys dispersed on the surface of the nanosized H $\beta$  zeolite provided better activity for methane decomposition. A maximum methane conversion of ~33% was achieved over 20%Ni–5%Cu/nano H $\beta$  zeolite catalyst in the first 60 min of time in stream at 550 °C with a methane flow rate of 30 ml/min. However, with increasing time on stream a drastic decrease in the methane conversion was observed, and it was found to be completely deactivated at 720 min of time on stream.

Awadallah et al. [30] reported methane decomposition over Cr-, Mo- and W- based Co/MgO bimetallic catalysts. They reported maximum methane conversions of 88%, 76%, 79% and 77% for the Co, Co–Cr, Co–Mo and Co–W/MgO catalysts respectively in the first

5 min of time on stream. No deactivation was observed for the catalysts, for a period of 420 min of time on stream. The high catalytic stability of the catalysts was due to the dispersion and stabilization of cobalt species on the MgO support. Al-Fatesh et al. [80] used alumina supported Fe and Ni–Fe bimetallic catalysts for methane decomposition and the effects of the synthesis method and annealing temperatures were studied. As per their report, steady state hydrogen yields of ~60% and 65% was observed at 700 °C, with a methane/nitrogen ratio of 1.5/1, a total flow rate of 25 ml/min and a space velocity of 5000 ml/hg, for the 20%Fe/Al<sub>2</sub>O<sub>3</sub> and 5%Ni–Fe/Al<sub>2</sub>O<sub>3</sub> catalysts respectively, prepared by an impregnation method and calcined at 500 °C. All of the catalysts showed high catalytic stability for a period of 180 min of time on stream. Shen and Lua [81] reported Ni/TiO<sub>2</sub> catalysts prepared by a sol gel method for methane decomposition. They reported that a highest carbon yield of 321.1 gC/g Ni was obtained for the 1NiO–2TiO<sub>2</sub> catalyst at 500 °C.

In another work, Awadallah et al. [82] compared a set of silica supported 40% nickel catalysts for methane decomposition. They used ZSM-5(25), ZSM-5(400) and amorphous silica (AS) as the catalyst supports, and nickel was loaded into it by an impregnation method. Irrespective of the support material, a maximum initial hydrogen yield of 77% was achieved for all of the catalysts, followed by a decrease of the hydrogen yield, to various extents based on the nature of the support. Of the three Ni/ZSM-400 catalyst exhibited the highest catalytic stability, since a final hydrogen yield of ~62% was noted for the catalyst at the end of 180 min of time on stream. The high catalytic stability of the Ni/ZSM-400 catalyst could be due to the existence of highly dispersed metal particles on the catalyst support. Lua and Wang [3] reported methane decomposition over a set of Ni–Cu–Co alloy particles prepared by the thermal decomposition of fibrous Ni–Cu–Co oxalate precursors. They reported that all of the ternary alloy catalysts with various compositions of metals showed high catalytic activity in the initial stage of reaction until 750 °C, and 800 °C is the maximum reaction temperature, at which the ternary alloys showed the highest activity, since above 800 °C, a rapid drop in the catalytic activity was noticed. Moreover, all of the ternary alloy catalysts exhibited steady state catalytic stability for a period of 300 min of time on stream, at various reaction temperatures. Fakirah et al. [83] studied methane decomposition over Fe loaded MgO and TiO<sub>2</sub> catalysts prepared by an impregnation and co-precipitation method and reported that approximately 45% hydrogen yield was obtained for the 30%Fe/MgO catalyst, whereas low catalytic activity with a hydrogen yield of 5% was noticed for the TiO<sub>2</sub> supported catalyst. However, the Fe/MgO catalyst prepared by the co-precipitation method showed a higher hydrogen yield of 65% for 180 min of time on stream.

Ibrahim et al. [84] studied methane decomposition over iron loaded alumina catalysts prepared by a co-precipitation method. As per their report, a maximum hydrogen yield of ~77% was obtained for the 60%Fe/Al<sub>2</sub>O<sub>3</sub> catalyst at 700 °C. Moreover, with increasing iron loading from 35 to 80%, the hydrogen yield was found to be increased. The catalysts were found to be stable for a period of 240 min of time on stream. Ahmed et al. [85] studied methane decomposition over 50% Ni/CeO<sub>2</sub>–Al<sub>2</sub>O<sub>3</sub> catalyst with different loadings of ceria. They found that their catalytic performance was completely governed by the amount of ceria in the catalysts.

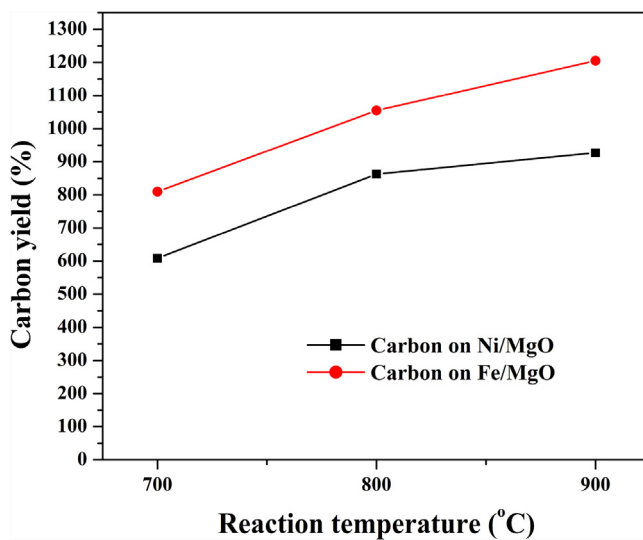


**Fig. 10.** Carbon yield at various reaction temperatures over Ni/MgO and Fe/MgO catalysts.

However, a maximum hydrogen yield of ~53% was attained for the Ni/Ce<sub>25</sub>-Al<sub>75</sub> catalyst at 700 °C. However, no catalyst deactivation was observed for the catalysts for a period of 390 min of time on stream, due to the presence of highly dispersed nickel nanoparticles on the CeO<sub>2</sub> support, formed by the reduction of the Ni-O-Ce solid solution. Zhou et al. [86] reported methane decomposition over Fe/Al<sub>2</sub>O<sub>3</sub> catalyst prepared by a fusion and impregnation method. They reported that irrespective of the preparation method and iron loading, the Fe/Al<sub>2</sub>O<sub>3</sub> catalyst exhibited the best catalytic performance for methane decomposition. As per their report, the catalyst prepared by the fusion method with 65% Fe content, reduced at 750 °C with hydrogen, showed high catalytic activity and stability for methane decomposition. A maximum steady state methane conversion of 70% was observed for the catalyst at 750 °C with a space velocity of 1.875 l/hg.

From the above discussion, it could be said that, all of the aforementioned catalysts were highly active and stable for the decomposition of methane. However, many of the catalysts used for the reaction were found to be prepared with high metal loading and used several tedious reaction conditions for the synthesis. Moreover, diluted methane with low flow rates was used in the reaction. By considering these points, the one-pot sol-gel derived MgO supported nickel and iron catalysts showed competent activity and stability for undiluted methane decomposition with a flow rate of 150 ml/min, with some of the reported catalysts.

### 3.3. Characterization of carbon deposited catalysts

The yields of nanocarbon deposited over MgO supported Ni and Fe nanocatalysts at various reaction temperatures were calculated. As shown in Fig. 10, the yield of nanocarbon increased significantly with increasing reaction temperatures over both of the catalysts. The carbon yield was calculated to be 608%, 863% and 927% for the Ni/MgO catalyst and 810%, 1055% and 1205% for the Fe/MgO catalyst at 700 °C, 800 °C and 900 °C, respectively. The highest carbon yield was observed for the Fe/MgO catalyst at all of the reaction temperatures. This could be attributed to the highest initial activity of the Fe/MgO catalyst for methane decomposition (Fig. 9). Compared to the Ni/MgO catalyst, more catalytic activity was shown by the Fe/MgO catalyst, which is directly contributed to the high yield of nanocarbon. Thus, the carbon yield follows the catalyst order of Fe/MgO > Ni/MgO and the reaction temperature order of 900 °C > 800 °C > 700 °C, respectively.

The nanocarbon deposited catalysts were characterized using XRD analysis to determine their crystalline and structural properties. Fig. 11 shows the XRD patterns of the spent catalysts after methane decomposition at various reaction temperatures. Fig. 11(a) represents the XRD patterns of the nanocarbon deposited over Ni/MgO catalyst. The first well resolved intense diffraction peak centered at the 2θ value of 26.6° with the (002) plane was attributed to the formation of graphitic carbon. In addition to crystalline carbon, several catalytic peaks were also detected. As seen in the fresh catalyst, the diffraction peaks centered at the 2θ values of 36.86°, 43°, 62.34°, 74.57° and 78.53° were indexed to the existence of the NiMgO solid solution in the spent catalysts. The phase segregation of NiMgO solid solution into pure MgO and NiO cannot be discarded since their peaks were quite similar to those of the solid solution. The other well resolved diffraction peaks observed at the 2θ values of 44.43°, 51.73° and 76.21° were directly indexed to the existence of metallic phase of nickel in the spent catalysts. The metallic nickel particles could be formed by the reduction of the NiMgO solid solution either by the direct reduction or by the decomposition. The average crystalline size of the nickel particles calculated using Scherrer's equation was found to be approximately

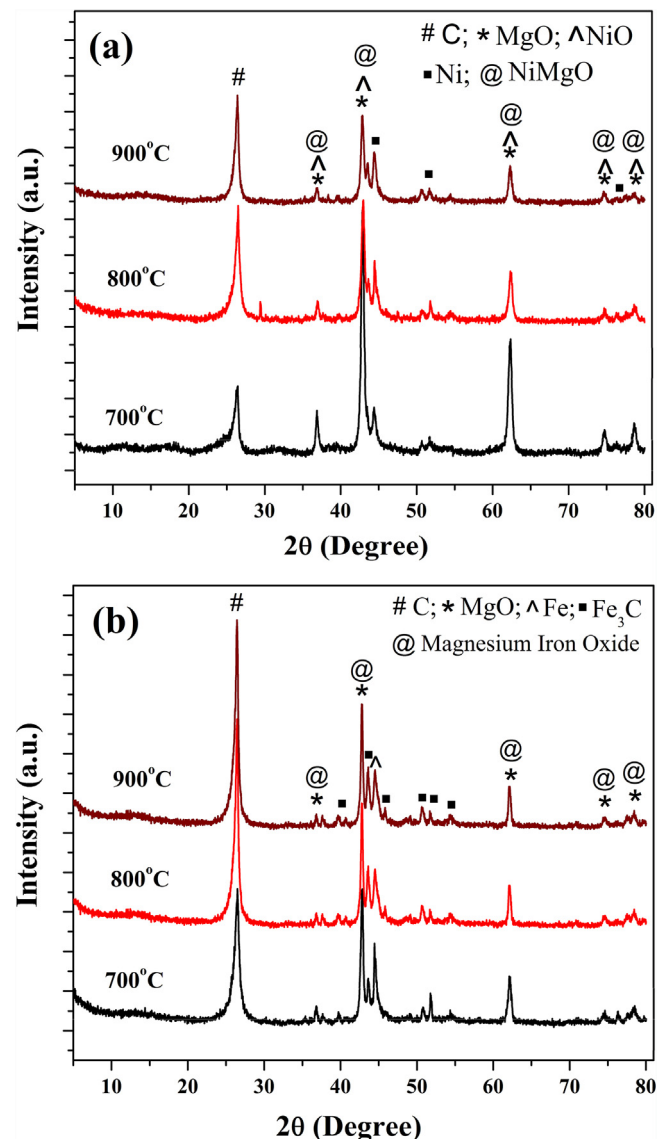


**Fig. 11.** X-ray diffraction patterns of the spent catalysts after methane decomposition at various reaction temperatures over (a) Ni/MgO and (b) Fe/MgO catalysts.

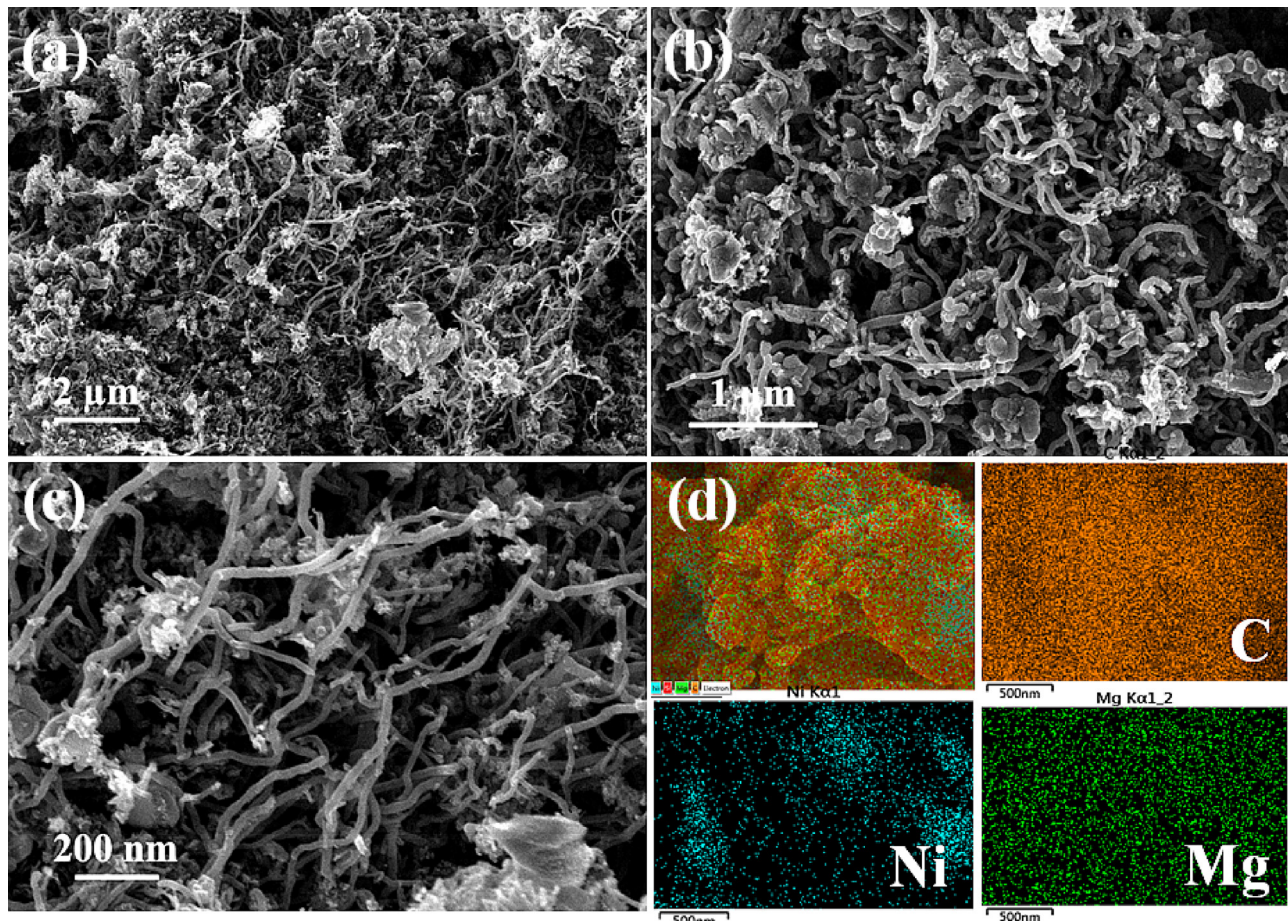


**Fig. 12.** FESEM images (a–c) and mapping analysis (d) of the nanocarbon deposited over Ni/MgO.

5–6 nm at all of the studied reaction temperatures. Thus, the catalytic activity and stability of the Ni/MgO catalyst could be ascribed to the existence of these small metallic nickel particles, which are expected to be finely dispersed on the surface of the catalyst for the continuation of the reaction without any significant deactivation. This is quite related to the previous results [72,73]. Moreover, it can be clearly observed that, the intensity difference of the diffraction peaks related to the metallic nickel was not much significant with respect to the reaction temperatures, just like the other diffraction peaks in the spent catalysts. This could be the reason for their similar catalytic activities for methane decomposition, irrespective of the reaction temperatures. However, when increasing the reaction temperature from 700 °C to 900 °C, the carbon peak intensity was significantly increased. This could be attributed to the increased crystallinity of the carbon deposited at high reaction temperatures. Furthermore, the intensity of the peaks corresponding to the NiMgO solid solution was decreased with increasing reaction temperature, which could be attributed to the increased yield of nanocarbon at high reaction temperatures. A direct correlation was observed here for the carbon yield with the peak intensity. While comparing the intensities of the peaks of crystalline carbon and the NiMgO solid solution (peak at the 2θ value of 43°), it is found that, at 700 °C, the highest peak intensity was exhibited by the solid solution and hence a low carbon yield. At 800 °C, both of the peaks showed almost the same intensity. However, the peak intensity of crystalline carbon was found to be high at 900 °C, while the intensity of the NiMgO solid solution was low at 900 °C. It indicates the bulk surface deposition of the nanocarbon at high reaction temperatures. The interlayer d-spacing of the crystalline carbon was

calculated (at the 2θ value of ~26°) and found to be 0.3391 nm, 0.3365 nm, and 0.3408 nm for the carbon over the Ni/MgO catalyst at 700 °C, 800 °C and 900 °C respectively. This indicates the higher crystalline quality of the carbon, since these values are very close to the ideal distance between two graphitic layers (0.3354 nm) [87].

The XRD patterns of the carbon deposited Fe/MgO catalysts after methane decomposition are shown in Fig. 11(b). As shown, the intense diffraction peak at the 2θ value of 26.6° with the (002) plane was related to the formation of crystalline carbon. The other diffraction peaks centered at the 2θ values of 36.52°, 42.75°, 62.24°, 74.57° and 78.53° corresponded to the existence of magnesioferrites/MgO. The diffraction peak observed at the 2θ value of 44.43° in the spent catalysts was attributed to existence of the crystalline structure of metallic iron, which could be formed by the reduction of magnesioferrites under the applied reduction process. The other well-resolved less intense peaks observed in the spectra were attributed to the formation of iron carbide (Fe<sub>3</sub>C) via the thermal interaction of iron with formed carbon. Moreover, it is worth to mention that, the intensity of the carbon peak over the Fe/MgO catalyst at all of the reaction temperatures was significantly higher than that of the same over the Ni/MgO catalyst. It could be attributed to the high yield of nanocarbon over the iron catalyst, in addition to its improved crystallinity. Moreover, the carbon peak intensity was observed to be considerably higher than that of the peak related to magnesioferrites at 800 °C and 900 °C whereas the intensities were quite similar at 700 °C. It was reported that the higher the carbon peak intensity is, the higher the degree of crystallization is [88]. The crystalline size of metallic iron was calculated to be ~9–10 nm at 700 °C whereas a quite smaller crystalline size of ~4–5 nm was

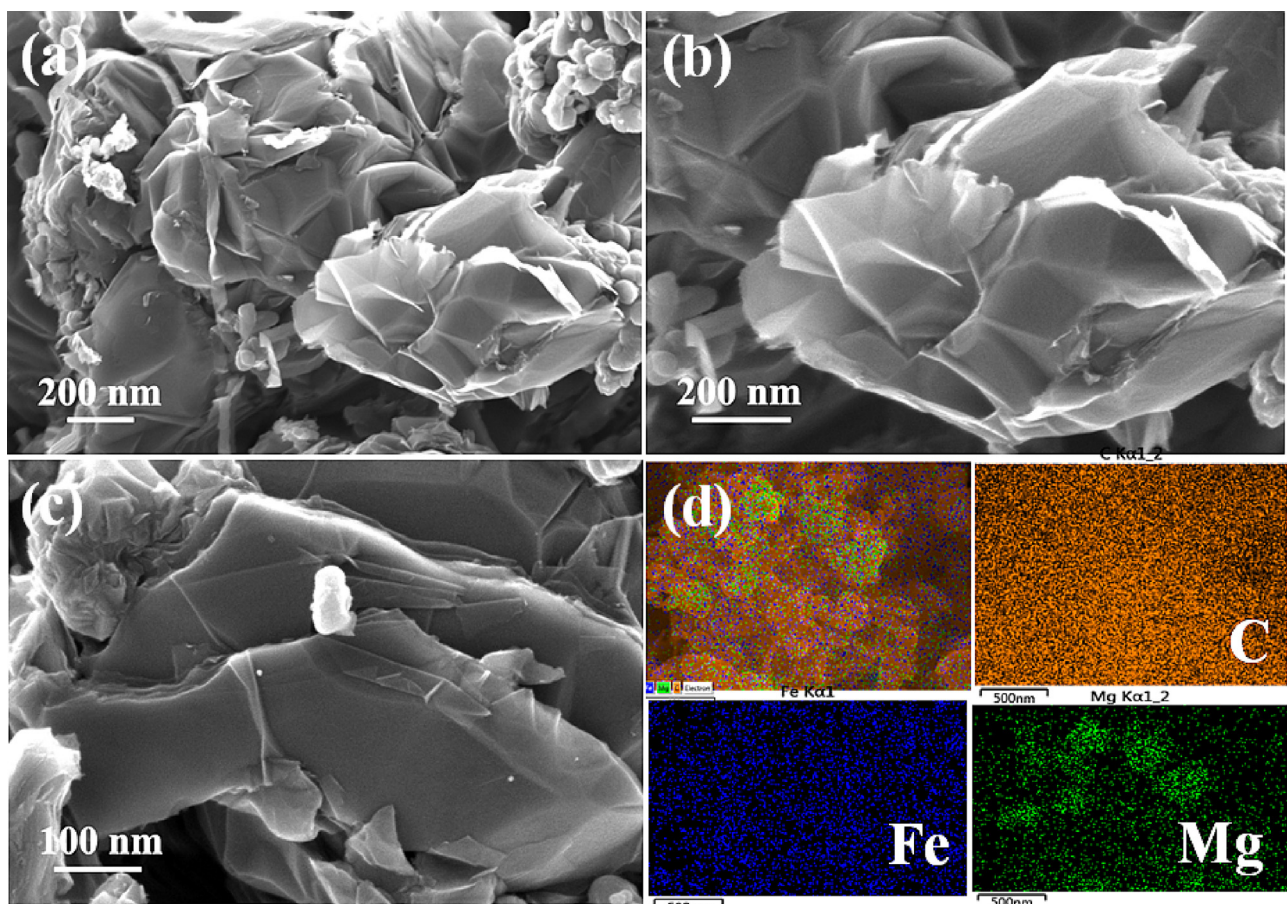


**Fig. 13.** FESEM images (a–c) and mapping analysis (d) of the nanocarbon deposited over Fe/MgO.

observed for the iron at 800 °C and 900 °C. This could be due to the dispersion of iron particles on the nanocarbon, which expect to decrease the crystallinity. Thus, the activity and stability of the Fe/MgO catalyst could be attributed to the presence of these smaller iron nanoparticles dispersed on the catalyst surface, formed by the reduction of magnesioferrites. From the observation, it is clear that the stability of the MgO supported Ni and Fe catalysts against deactivation was attributed to the presence of the active phase of metallic nickel and iron in the spent catalysts, which is expected to be finely dispersed on the hardly reduced solid solutions. Compared to the NiMgO solid solution, the magnesioferrites actively participated in the reaction since they are more reduced than the NiMgO solid solution and a temperature dependence was noticed for the crystalline size of the formed iron particles.

The morphological characterization of the nanocarbon deposited over nickel and iron catalysts supported on MgO was studied using FESEM analysis, and the results are shown in Figs. 12 and 13. Fig. 12 shows the FESEM images of the nanocarbon deposited over nickel catalyst after methane decomposition at 900 °C. Carbon nanotubes with irregular particles or agglomerates were observed, as shown in Fig. 12(a–c). The diameters of the carbon nanotubes were measured and found to vary from 30 to 60 nm in width. However, it is very hard to determine their actual length since they extended several micrometers and were interwoven. Cracked carbon nanotubes were also visible. The existence of carbon nanotubes with open ended tips could be attributed to the base mode growth of carbon due to the strong metal-support interaction. The irregular particles can be either catalyst encapsulated carbon particles or catalyst species. The size of the carbon particles was found to vary from ~20 nm to several

micrometers. The elemental mapping analysis shown in Fig. 12(d) confirms the bulk deposition of nanocarbon on the surface of the catalyst (mapping for O not shown). Compared to our previously reported supported Ni-based catalysts, the Ni/MgO catalyst did not produce bulk amount of carbon nanotubes [8,9,89]. The amount of carbon nanotubes is very small and an equal proportion of the irregular carbon agglomerates or chunks was also noticed. Similar types of observations were also reported for other types of catalysts [90,91].

Fig. 13 displays the FESEM images of the nanocarbon deposited Fe/MgO catalyst after methane decomposition at 900 °C. For the first time, instead of single-, double- or multiwalled carbon nanotubes over Fe based MgO catalysts reported in the literature [35–57], the bulk deposition of graphene sheets with a puffy appearance was observed over the sol-gel derived Fe/MgO catalysts. The formation of graphene sheets by the decomposition of methane over Fe/MgO catalysts has not yet been reported. The thin layers of graphene sheets and the aggregates of such layers are clearly displayed in Fig. 13(b, c). Moreover, the formed graphene sheets contain a large number of wrinkles and ripples. The elemental mapping shown in Fig. 13(d) confirms the formation of graphene sheets after methane decomposition. The actual mechanism for the formation of graphene sheets over iron based supported and unsupported catalysts is still unclear, and more research is on-going. It is expected that the high carbon diffusion coefficient (CDC) of metallic iron accelerates the precipitation of supersaturated carbon as graphene layers since the CDC of iron is reported to be three times higher than that of metallic nickel. Moreover, a few researchers have recently reported that, the formation of nanocarbon by methane decomposition over iron proceeds through the

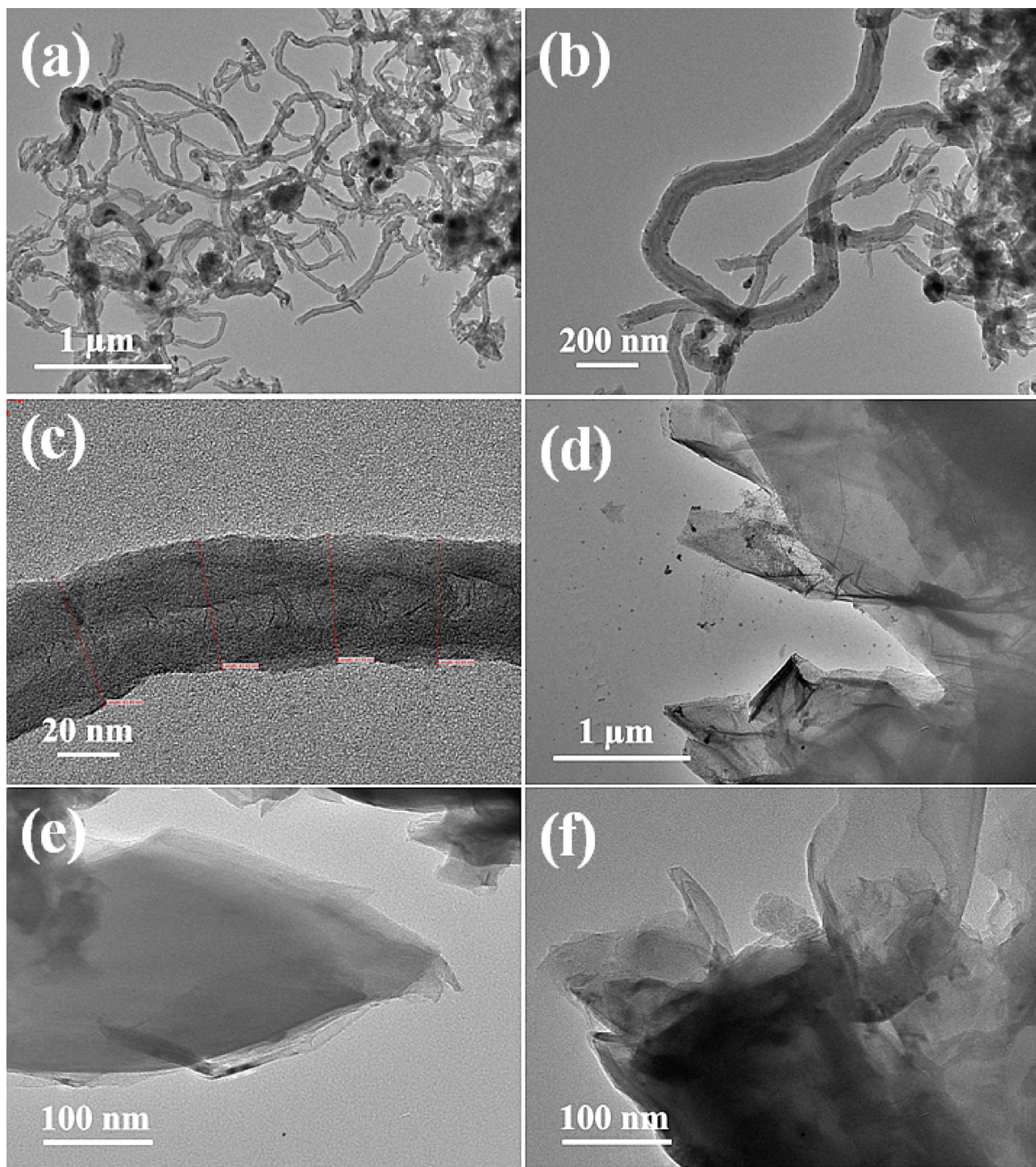


**Fig. 14.** TEM images of the nanocarbon deposited over (a–c) Ni/MgO and (d–f) Fe/MgO catalysts.

generation of iron carbide,  $\text{Fe}_3\text{C}$ , as detected in the XRD patterns of the spent catalysts [92,93]. Zhou et al. [86] reported a carbon growth mechanism over iron catalyst in methane decomposition. However, it is also not related to the formation of graphene layers. According to them, during the first stage of methane decomposition, the methane molecule decomposes to form hydrogen and amorphous carbon on the surface of the zero valent iron. Because of the body centered cubic crystal structure, interstitial configuration and dimension and low carbon solubility of metallic iron, the accommodation of the carbon on iron is not easy, as reported by Hasebe et al. [94] and Wirth et al. [95]. Therefore, as the amount

of carbon deposited by decomposition process increases, the solubility of carbon in iron decreases, and hence stable iron carbide is formed through the rearrangement of iron atoms [96]. The iron carbide was also reported to be catalyzing the methane decomposition. However, the bulk deposition of carbon on  $\text{Fe}_3\text{C}$ , triggers the formation of supersaturated iron carbide ( $\text{Fe}_3\text{C}_{1+x}$ ), which then decomposes into stoichiometric iron carbide and crystalline carbon. Moreover, the time interval between the formation of iron carbide and its spurt as graphitic carbon is less than a second, and it is not necessary to nucleate and grow as carbon nanotubes as reported by Sharma et al. [97]. Therefore, it is expected that the for-

mation of graphitic layers in this study proceeds through the same pathway. However, the morphology of the deposited carbon could be related to the physiochemical properties and composition of the catalysts, especially the geometry, interface, phase and energy factors of the metals and the reaction parameters as reported previously [6].

Recently, the formation of graphene sheets via methane decomposition was reported over a set of supported and unsupported catalysts. Shen and Lu [98] reported the methane decomposition as a facile and economical method for the scalable continuous synthesis of single-layered and few-layered graphene sheets over unsupported iron catalyst. A high yield of graphene was observed over unsupported iron catalysts. They reported that a maximum graphene deposit of 6 g per g of the iron catalyst was achieved with a feed flow rate of 25 ml/min under atmospheric pressure. Jana et al. [99] produced few layered graphene sheets by methane decomposition over cobalt-based unsupported catalysts prepared by a precipitation method in an ethylene glycol medium. As per their report, for the formation of graphene sheets, the catalyst was reduced in the presence of methane, since it is the crucial factor for its formation. Recently, Awadallah et al. [100] reported the bulk deposition of few-layered graphene nano-platelets via methane decomposition over unsupported Ni, Co and Fe nanosheets. As per their report, the number of layers in the graphene sheets was completely dependent on the morphology of the synthesized catalysts. A maximum graphene yield of 254% was achieved over the unsupported Ni catalyst for 120 min of decomposition reaction under atmospheric pressure. 233% graphene was deposited over the iron catalyst. The unsupported porous iron catalysts prepared by a precipitation method and a solid state citrate fusion method developed by our group also successfully produced graphene sheets by the catalytic decomposition of undiluted methane. The maximum yield of graphene was found to be 147% and 623%, respectively, for the precipitation- and fusion-derived iron catalysts [101,102]. Sol-gel derived silica microflakes supported iron catalyst also produced multi-layered graphene sheets via catalytic methane decomposition at 800 °C for a period of 300 min of reaction, and a final graphene yield of 177% was achieved over the catalyst [9].

To study the internal structure and wall/layer nature of the deposited carbon, TEM analysis was further studied, and the images are shown in Fig. 14. As shown in Fig. 14(a), both carbon nanotubes and metal catalyst encapsulated irregular carbon particles were deposited over the Ni/MgO catalyst. The dark spots indicate the presence of the catalyst/metallic portion in the spent catalyst. As shown, the diameters of the carbon nanotubes were found to vary between 30 nm to 55 nm, which is highly consistent with the SEM measurements. The high magnified TEM image of a carbon nanotube is shown in Fig. 14(c), which confirms the multi-wall nature of the deposited carbon nanotubes. The diameter of the multiwalled carbon nanotube shown in Fig. 14(c) was measured to be ~42 nm, with an outer wall thickness of 16 nm and an internal hollow channel space of 10 nm. The layered structure of graphene sheets is clearly seen in Fig. 14(d–f). The transparency of the sheets confirms the formation of few layered graphene sheets. The folding of the sheets is visibly observed in these images. The single layers of graphene sheets are observed to be stacked together and hence few layered structures resulted. The layer thickness was found to vary greatly.

To study the crystallinity and degree of graphitization of the deposited nanocarbon at various reaction temperatures, all of the samples were characterized using Raman spectroscopy, and the Raman spectra are shown in Fig. 15. Three well resolved Raman bands are observed in the Raman spectrum of each of the samples, for all of the reaction temperatures over both nickel and iron catalysts. The bands observed at nearly 1344 cm<sup>-1</sup>, 1571 cm<sup>-1</sup> and 2678 cm<sup>-1</sup> in the Raman spectrum were named the D band, G band

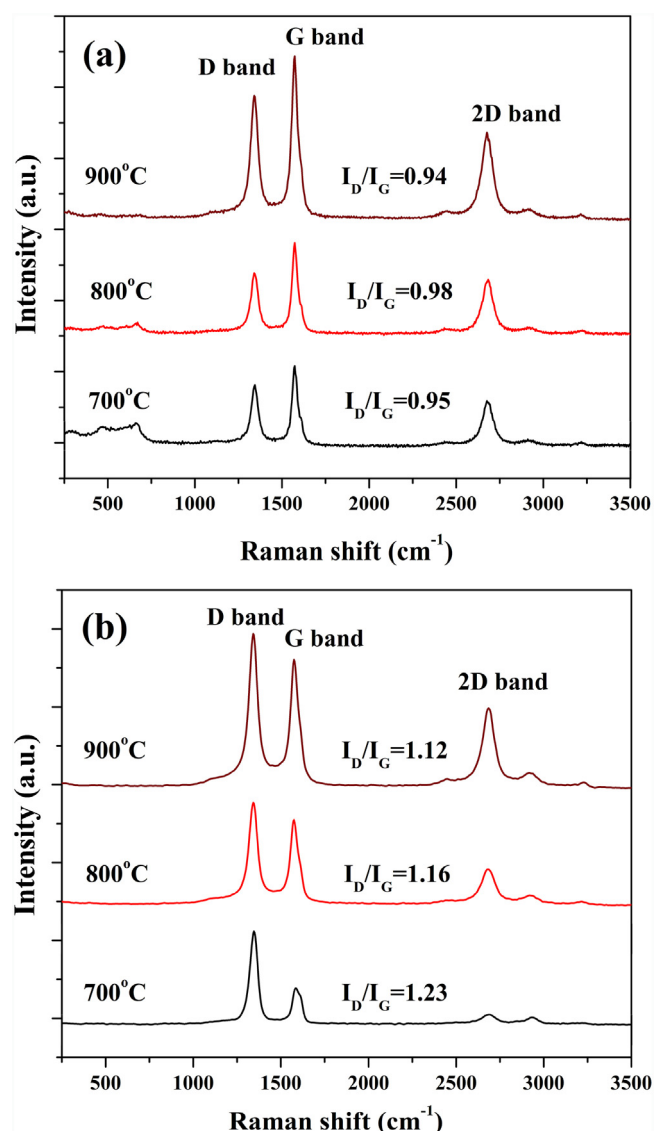


Fig. 15. Raman spectra of the carbon deposited over (a) Ni/MgO and (b) Fe/MgO catalysts at various reaction temperatures.

and 2D (G') band, respectively. These bands were identified as the characteristic bands of the graphitic carbon [103]. Over both of the catalysts, the band positions remained the same, irrespective of the reaction temperatures and the nature and morphology of the nanocarbon formed. The existence of structural disorders or imperfections on the graphitic layers was indicated by the D band. The G band was ascribed to the presence of in-plane or tangential mode stretching vibration of the sp<sup>2</sup> carbon atoms present in the graphitic layers of the nanocarbon [104]. The 2D band is a second-order two-phonon process related to the formation of graphene layers. It was found that with increasing reaction temperatures, the intensities of all of the Raman bands were increased over both of the catalysts. This could be attributed to the enhanced crystalline quality of the deposited carbon at high reaction temperatures.

Furthermore, to evaluate the graphitization degree and crystallinity of the nanocarbon, the intensity ratio of D and G bands were calculated. The  $I_D/I_G$  values were found to be 0.95, 0.98 and 0.94 for the carbon deposited over the Ni/MgO catalyst and 1.23, 1.16 and 1.12 for the carbon deposited over the Fe/MgO catalyst at 700 °C, 800 °C and 900 °C, respectively. The values were close to unity, indicating that the carbon samples were highly crystal-

lized and graphitized. However, the  $I_D/I_G$  values were found to be decrease with increasing reaction temperatures over both the NiMgO and Fe/MgO catalysts. This indicates that, with increasing reaction temperature, the crystallinity and graphitization degree of the nanocarbon increase [105]. In the present case, lower  $I_D/I_G$  values were observed for the nanocarbon deposited over the Ni/MgO catalyst compared to the Fe/MgO catalyst, indicating the higher graphitization degree and crystalline quality [60]. Moreover, the intensity of the D band was quite lower than the intensity of the G band for the carbon deposited over Ni/MgO catalyst whereas the intensity of the D band was quite higher than the same for Fe/MgO catalyst. It clearly indicates that the Ni/MgO catalyst produced nanocarbon with low structural imperfections compared to the Fe/MgO catalyst. The intensity of the G band and 2D band was further used to confirm the formation of multi-layer graphene sheets. It was reported that, irrespective of the thickness of graphene sheets, an intense 2D band was observed for the disordered carbon nanomaterials [106]. However, an intense 2D band was observed for the single-layered graphene sheets. Thus the low intensity of the 2D band compared to the G band confirms the deposition of few layered graphene sheets [107].

#### 4. Conclusions

The nickel- and iron- loaded MgO catalysts were successfully synthesized via a facile one-pot sol-gel route and then, characterized and used for the thermocatalytic decomposition of undiluted methane. The formation of the NiMgO solid solution and magnesio-ferrites was observed in the fresh catalysts. A strong metal-support interaction was observed for the NiMgO solid solution compared to the magnesioferrites, as indicated by the hydrogen- temperature programmed reduction analysis. The surface area of the MgO support was found to decrease after metal loading, due to the blocking of mesopores. The as-prepared catalysts were found to be highly active and stable for the decomposition of undiluted methane for a period of 360 min of reaction, without any severe catalyst deactivation. When increasing the reaction temperature from 700 °C to 900 °C, a small increase in the hydrogen yield was observed for the Ni/MgO catalyst. After 180 min of time on stream, the hydrogen yield remained more or less the same at all of the reaction temperatures. However, over the Fe/MgO catalyst, the initial hydrogen yield was observed to increase significantly with increasing reaction temperature, and stable activity was achieved after 150 min of time on stream. The presence of highly dispersed small nickel and iron crystals formed by the reduction of hardly reducible NiMgO and magnesioferrites could be responsible for the activity and stability of the catalysts. It was found that, with increasing reaction temperature, the yield of nanocarbon deposited also increased over both of the catalysts. However, the highest carbon yield was obtained over the Fe/MgO catalyst due to its better catalytic performance for the decomposition reaction. The morphological characterization of the nanocarbon indicated the deposition of multiwalled carbon nanotubes with carbon particles and few layered graphene sheets over the nickel and iron catalysts, respectively. The influence of reaction temperature on the crystalline properties of the deposited nanocarbon was studied in detail. It indicated that the crystallinity and graphitization degree of the deposited nanocarbon increased with increasing reaction temperature from 700 °C to 900 °C as confirmed by X-ray diffraction and Raman analysis.

#### Acknowledgements

This work was funded by Yayasan Sime Darby, Universiti Kebangsaan Malaysia and Sime Darby Research under grants PKT 6/2012 and KK-2014-014, respectively. The Center for Research

and Instrumentation Management (CRIM), UKM is acknowledged for providing the characterization of the materials. The Institut Teknologi Maju (ITMA) at Universiti Putra Malaysia (UPM) is acknowledged for providing the Raman analyses.

#### Appendix A. Supplementary data

Supplementary data associated with this article can be found, in the online version, at <http://dx.doi.org/10.1016/j.apcatb.2017.04.070>.

#### References

- [1] M. Pudukudy, Z. Yaakob, M. Mohammad, B. Narayanan, K. Sopian, Renewable hydrogen economy in Asia—opportunities and challenges: an overview, *Renew. Sustain. Energy Rev.* 30 (2014) 743–757.
- [2] Y. Ying, C. Meisheng, L. Minglai, Z. Na, L. Zhiqi, S. Yongxi, Rare earth modified Ni-Si catalysts for hydrogen production from methane decomposition, *J. Rare Earths* 32 (2014) 709–714.
- [3] A.C. Lua, H.Y. Wang, Hydrogen production by catalytic decomposition of methane over Ni-Cu-Co alloy particles, *Appl. Catal., B* 156–157 (2014) 84–93.
- [4] A.C. Lua, H.Y. Wang, Decomposition of methane over unsupported porous nickel and alloy catalyst, *Appl. Catal. B* 132–133 (2013) 469–478.
- [5] K.S. Han, J.H. Kim, H.K. Kim, K.T. Hwang, Direct methane cracking using a mixed conducting ceramic membrane for production of hydrogen and carbon, *Int. J. Hydrogen Energy* 38 (2013) 16133–16139.
- [6] Y. Li, D. Li, G. Wang, Methane decomposition to CO<sub>x</sub>-free hydrogen and nano-carbon material on group 8–10 base metal catalysts: a review, *Catal. Today* 162 (2011) 1–48.
- [7] Y. Shen, A.C. Lua, Polyol synthesis of nickel-copper based catalysts for hydrogen production by methane decomposition, *Int. J. Hydrogen Energy* 40 (2015) 311–321.
- [8] M. Pudukudy, Z. Yaakob, M.S. Takriff, Methane decomposition into CO<sub>x</sub> free hydrogen and multiwalled carbon nanotubes over ceria, zirconia and lanthana supported nickel catalysts prepared via a facile solid state citrate fusion method, *Energy Convers. Manage.* 126 (2016) 302–315.
- [9] M. Pudukudy, Z. Yaakob, Methane decomposition over Ni, Co and Fe based monometallic catalysts supported on sol gel derived SiO<sub>2</sub> microflakes, *Chem. Eng. J.* 262 (2015) 1009–1021.
- [10] I.V. Mishakov, A.F. Bedilo, R.M. Richards, V.V. Chesnokov, A.M. Volodin, V.I. Zaikovskii, et al., Nanocrystalline MgO as a dehydro-halogenation catalyst, *J. Catal.* 206 (2002) 40–48.
- [11] C. Shi, P. Zhang, Role of MgO over  $\gamma$ -Al<sub>2</sub>O<sub>3</sub>-supported Pd catalysts for carbon dioxide reforming of methane, *Appl. Catal. B* 170–171 (2015) 43–52.
- [12] L. Kaluža, D. Gulkova, Z. Vít, M. Zdražil, High-activity MgO-supported CoMo hydro desulfurization catalysts prepared by non-aqueous impregnation, *Appl. Catal. B* 162 (2015) 430–436.
- [13] S.W. Liu, J. Weaver, Z. Yuan, W. Donner, C.L. Chen, J.C. Jiang, E.I. Meletis, et al., Ferroelectric (Pb, Sr) TiO<sub>3</sub> (Pb, Sr) TiO<sub>3</sub> epitaxial thin films on (001) MgO for room temperature high-frequency tunable microwave elements, *Appl. Phys. Lett.* 87 (2005), 142905/1.
- [14] R.K. Singh, A. Yadav, A. Agrawal, A. Shukla, Sh. Adak, T. Sasaki, R. Bal, Synthesis of highly coke resistant Ni nanoparticles supported MgO/ZnO catalyst for reforming of methane with carbon dioxide, *Appl. Catal. B* 191 (2016) 165–178.
- [15] H. Mirzaei, A. Davoodnia, Microwave assisted sol-gel synthesis of MgO nanoparticles and their catalytic activity in the synthesis of hantzsch 1,4-dihydropyridines, *Chin. J. Catal.* 33 (2012) 1502–1507.
- [16] C. Shi, P. Zhang, Role of MgO over Al<sub>2</sub>O<sub>3</sub>-supported Pd catalysts for carbon dioxide reforming of methane, *Appl. Catal. B: Environ.* 170–171 (2015) 43–52.
- [17] X. Luo, Y. Hong, F. Wang, S. Hao, C. Pang, E. Lester, T. Wu, Development of nano Ni<sub>x</sub>Mg<sub>1-x</sub>O solid solutions with outstanding anti-carbon deposition capability for the steam reforming of methanol, *Appl. Catal. B* 194 (2016) 84–97.
- [18] Z. Boukha, C.J. González, M.G. Calvo, B. de Rivas, J.R.G. Velasco, J.I.G. Ortiz, R.L. Fonseca, MgO/NiAl<sub>2</sub>O<sub>4</sub> as a new formulation of reforming catalysts: tuning the surface properties for the enhanced partial oxidation of methane, *Appl. Catal. B* 199 (2016) 372–383.
- [19] S.D. Stefanidis, S.A. Karakoula, K.G. Kalogiannis, E.F. Iliopoulos, A. Delimitis, H. Yiannoulakis, T. Zampetakis, A.A. Lappas, K.S. Triantafyllidis, Natural magnesium oxide (MgO) catalysts: a cost-effective sustainable alternative to acid zeolites for the in situ upgrading of biomass fast pyrolysis oil, *Appl. Catal. B* 196 (2016) 155–173.
- [20] F. Bimbela, J. Ábrego, R. Puerta, L. García, J. Arauzo, Triantafyllidis Catalytic steam reforming of the aqueous fraction of bio-oil using Ni-Ce/Mg-Al catalysts, *Appl. Catal. B* 15 (2017) 346–357.
- [21] L. Xu, H. Song, L. Chou, Carbon dioxide reforming of methane over ordered mesoporous NiO-MgO-Al<sub>2</sub>O<sub>3</sub> composite oxides, *Appl. Catal. B* 108–109 (2011) 177–190.
- [22] A.M. Cassell, J.A. Raymakers, J. Kong, H.J. Dai, Large scale CVD synthesis of single-walled carbon nanotubes, *J. Phys. Chem. B* 103 (1999) 6484–6492.

[23] S. Tang, Z. Zhong, Z. Xiong, L. Sun, L. Liu, J. Lin, Z.X. Shen, K.L. Tan, Controlled growth of single-walled carbon nanotubes by catalytic decomposition of  $\text{CH}_4$  over Mo/Co/MgO catalysts, *Chem. Phys. Lett.* 350 (2001) 19–26.

[24] L. Ni, K.J. Kuroda, L.P. Zhou, T. Kizuka, K. Ohta, K. Matsuishi, J.J. Nakamura, Kinetic study of carbon nanotube synthesis over Mo/Co/MgO catalysts, *Carbon* 44 (2006) 2265–2272.

[25] A.E. Awadallah, A.A. Aboul-Enein, D.S. El-Desouki, A.K. Aboul-Gheit, Catalytic thermal decomposition of methane to  $\text{CO}_x$ -free hydrogen and carbon nanotubes over MgO supported bimetallic group VIII catalysts, *Appl. Surf. Sci.* 296 (2014) 100–107.

[26] R. Borghesi, A. Karimzadeh, N. Rashidi, Kinetics of methane decomposition to  $\text{CO}_x$ -free hydrogen and carbon nanofiber over Ni–Cu/MgO catalyst, *Int. J. Hydrogen Energy* 35 (2010) 9479–9488.

[27] J.L. Torres, M.J. Pinilla, R. Lázaro, I. Moliner, Hydrogen and multiwall carbon nanotubes production by catalytic decomposition of methane: thermogravimetric analysis and scaling-up of Fe–Mo catalysts, *Int. J. Hydrogen Energy* 39 (2014) 3698–3709.

[28] J.L. Pinilla, R. Utrilla, M.J. Lázaro, R. Moliner, I. Suelves, A.B. García, Ni- and Fe-based catalysts for hydrogen and carbon nanofilaments production by catalytic decomposition of methane in a rotary bed reactor, *Fuel Process. Technol.* 92 (2011) 1480–1488.

[29] J.L. Pinilla, I. Suelves, M.J. Lazar, R. Moliner, J.M. Palacios, Influence of nickel crystal domain size on the behaviour of Ni and NiCu catalysts for the methane decomposition reaction, *Appl. Catal. A* 363 (2009) 199–207.

[30] A.E. Awadallah, A.A. Aboul-Enein, A.K. Aboul-Gheit, Impact of group VI metals addition to Co/MgO catalyst for non-oxidative decomposition of methane into  $\text{CO}_x$ -free hydrogen and carbon nanotubes, *Fuel* 129 (2014) 27–36.

[31] M.A. Ermakova, D.Y. Ermakov, G.G. Kushinov, Effective catalysts for direct cracking of methane to produce hydrogen and filamentous carbon. Part I. Nickel catalysts, *Appl. Catal. A* 201 (2000) 61–70.

[32] G.Q. Ning, F. Wei, Q. Wen, G.H. Luo, Y. Wang, Y. Jin, Improvement of Fe/MgO catalysts by calcination for the growth of single- and double-walled carbon nanotubes, *J. Phys. Chem. B* 110 (2006) 1201–1205.

[33] S. Takenaka, H. Ogihara, I. Yamanaka, K. Otsuka, Decomposition of methane over supported-Ni catalysts: effects of the supports on the catalytic lifetime, *Appl. Catal. A* 217 (2001) 101–110.

[34] S. Takenaka, M. Ishida, M. Serizawa, E. Tanabe, K. Otsuka, Formation of carbon nanofibers and carbon nanotubes through methane decomposition over supported cobalt catalysts, *J. Phys. Chem. B* 108 (2004) 11464–11472.

[35] S.G. Kang, K.K. Cho, K.W. Kim, G.B. Cho, Catalytic growth of single- and double-walled carbon nanotubes from Fe–Mo nanoparticles supported on MgO, *J. Alloys Compds.* 449 (2008) 269–273.

[36] Q.W. Li, H. Yan, Y. Cheng Yan, J. Zhang, Z.F. Liu, A scalable CVD synthesis of high-purity single-walled carbon nanotubes with porous MgO as support material, *J. Mater. Chem.* 12 (2002) 1179–1183.

[37] Y. Jin, G. Wang, Y. Li, Catalytic growth of high quality single-walled carbon nanotubes over a Fe/MgO catalyst derived from a precursor containing Feitknecht compound, *Appl. Catal. A* 445–446 (2012) 121–127.

[38] W.M. Yeoh, K.Y. Lee, S.P. Chai, K.T. Lee, A.R. Mohamed, The role of molybdenum in Co–Mo/MgO for large-scale production of high quality carbon nanotubes, *J. Alloys Compd.* 493 (2010) 539–543.

[39] M.L. Wan, Y. Jia, F. Fang, S.S. Zhou, P.Y. Wu, D.Y. Peng, Synthesis of single- and double-walled carbon nanotubes using the calcined MgO supported commercial metal oxide as catalysts, *Thin Solid Films* 525 (2012) 35–39.

[40] S. Douven, S.L. Pirard, G. Heyen, D. Toye, J.P. Pirard, Kinetic study of double-walled carbon nanotube synthesis by catalytic chemical vapour deposition over an Fe–Mo/MgO catalyst using methane as the carbon source, *Chem. Eng. J.* 175 (2011) 396–407.

[41] A. Rashidi, R. Lotfi, E. Fakhrmosavi, M. Zare, Production of single-walled carbon nanotubes from methane over Co–Mo/MgO nanocatalyst: a comparative study of fixed and fluidized bed reactors, *J. Nat. Gas Chem.* 20 (2011) 372–376.

[42] W.M. Yeoh, K.Y. Lee, S.P. Chai, K.T. Lee, A.R. Mohamed, Effective synthesis of carbon nanotubes via catalytic decomposition of methane: influence of calcination temperature on metal-support interaction of Co–Mo/MgO catalyst, *J. Phys. Chem. Solids* 74 (2013) 1553–1559.

[43] H. Ago, K. Nakamura, N. Uehara, M. Tsuji, Roles of metal-support interaction in growth of single- and double-walled carbon nanotubes studied with diameter-controlled iron particles supported on MgO, *J. Phys. Chem. B* 108 (2004) 18908–18915.

[44] J.F. Colomer, C. Stephan, S. Lefrant, G.V. Tendeloo, I. Willems, Z. Konya, A. Fonseca, C. Laurent, J.B. Nagy, Large-scale synthesis of single-wall carbon nanotubes by catalytic chemical vapor deposition (CCVD) method, *Chem. Phys. Lett.* 317 (2000) 83–89.

[45] A. Govindaraj, E. Flahaut, C. Laurent, A. Peigney, A. Rousset, C.N.R. Rao, An investigation of carbon nanotubes obtained from the decomposition of methane over reduced  $\text{Mg}_{1-x}\text{M}_x\text{Al}_2\text{O}_4$  spinel catalysts, *J. Mater. Res.* 14 (1999) 2567–2576.

[46] W.W. Liu, A. Aziz, S.P. Chai, A.R. Mohamed, C.T. Tye, The effect of carbon precursors (methane, benzene and camphor) on the quality of carbon nanotubes synthesized by the chemical vapour decomposition, *Physica E* 43 (2011) 1535–1542.

[47] N. Abdullahi, J.E. Sakulchaicharoen, Selective synthesis of single-walled carbon nanotubes on Fe–MgO catalyst by chemical vapor deposition of methane, *Diamond Relat. Mater.* 41 (2014) 84–93.

[48] N. Abdullahi, J.E. Sakulchaicharoen, Selective growth of single-walled carbon nanotubes over Co–MgO catalyst by chemical vapor deposition of methane, *Diamond Relat. Mater.* 38 (2013) 1–8.

[49] G.Q. Ning, Y. Liu, F. Wei, Q. Wen, G.H. Luo, Porous and lamella-like Fe/MgO catalysts prepared under hydrothermal conditions for high-yield synthesis of double-walled carbon nanotubes, *J. Phys. Chem. C* 111 (2007) 1969–1975.

[50] J.Q. Nie, W.Z. Qian, Q. Zhang, Q. Wen, F. Wei, Very high-quality single-walled carbon nanotubes growing using a structured and tunable porous Fe/MgO catalyst, *J. Phys. Chem. C* 113 (2009) 20178–20183.

[51] Z.L. Li, J.A. Larsson, P. Larsson, R. Ahuja, J.M. Tobin, J.P. O'Byrne, M.A. Morris, G. Attard, J.D. Holmes, Copper/molybdenum nanocomposite particles as catalysts for the growth of bamboo-structured carbon nanotubes, *J. Phys. Chem. C* 112 (2008) 12201–12206.

[52] J.P. O'Byrne, Z. Li, J.M. Tobin, J.A. Larsson, P. Larsson, R. Ahuja, J.D. Holmes, Growth of carbon nanotubes from heterometallic palladium and copper catalysts, *J. Phys. Chem. C* 114 (2010) 8115–8119.

[53] H. Ago, N. Uehara, N. Yoshihara, M. Tsuji, M. Yumura, N. Tomonaga, T. Setoguchi, Gas analysis of the CVD process for high yield growth of carbon nanotubes over metal-supported catalysts, *Carbon* 44 (2006) 2912–2918.

[54] R. Chen, Y. Xie, Y. Zhou, J. Wang, H. Wang, Production of hydrogen-rich gas and multi-walled carbon nanotubes from ethanol decomposition over molybdenum modified Ni/MgO catalysts, *J. Energy Chem.* 23 (2014) 244–250.

[55] A. Izadi, M. Rashidi, R. Borghesi, A. Karimzadeh, Synthesis of carbon nanofibres over nanoporous Ni–MgO catalyst: influence of the bimetallic Ni–(Cu, Co, Mo) MgO catalysts, *J. Exp. Nanosci.* 7 (2012) 160–173.

[56] X. Yan, Ch. Liu, Effect of the catalyst structure on the formation of carbon nanotubes over Ni/MgO catalyst, *Diamond Relat. Mater.* 31 (2013) 50–57.

[57] K. Li, G. Lu, J.F. Liu, Synthesis of carbon nanotubes by catalytic decomposition of methane over Sm modified Ni–MgO catalysts, *Chin. J. Inorg. Chem.* 21 (2005) 1571–1575.

[58] M. Pudukudy, Z. Yaakob, Z.S. Akmal, Direct decomposition of methane over SBA-15 supported Ni: co and Fe based bimetallic catalysts, *Appl. Surf. Sci.* 330 (2015) 418–430.

[59] M. Pudukudy, Z. Yaakob, Z.S. Akmal, Direct decomposition of methane over Pd promoted Ni/SBA-15 catalysts, *Appl. Surf. Sci.* 353 (2015) 127–136.

[60] M. Pudukudy, Z. Yaakob, M.S. Takriff, Methane decomposition over unsupported mesoporous nickel ferrites: effect of reaction temperature on the catalytic activity and properties of the produced nanocarbon, *RSC Adv.* 6 (2016) 68081–68091.

[61] K. Maneerung, S. Hidajat, Co-production of hydrogen and carbon nanofibers from catalytic decomposition of methane over  $\text{LaNi}_{(1-x)}\text{M}_x\text{O}_3$   $\alpha$ -perovskite (where M = Co, Fe and X = 0, 0.2, 0.5, 0.8, 1), *Int. J. Hydrogen Energy* 40 (2015) 13399–13411.

[62] H.J. Jeong, K.H. An, S.C. Lim, M.S. Park, J.S. Chang, S.E. Park, S.J. Eum, et al., Narrow diameter distribution of single walled carbon nanotubes grown on Ni–MgO by thermal chemical vapor deposition, *Chem. Phys. Lett.* 380 (2003) 263–268.

[63] L.X. Li, D. Xu, X.Q. Li, W.C. Liu, Y. Jia, Excellent fluoride removal properties of porous hollow MgO microspheres, *New J. Chem.* 38 (2014) 5445–5452.

[64] K.V. Das, R.R. Devi, A.J. Thakur, Recyclable, highly efficient and low cost nano-MgO for amide synthesis under SFRC: a convenient and greener 'NOSE' approach, *Appl. Catal. A* 456 (2013) 118–125.

[65] H.X. Niu, Q. Yang, K.B. Tang, Y. Xie, Large-scale synthesis of single-crystalline MgO with bone-like nanostructures, *J. Nanopart. Res.* 8 (2006) 881–888.

[66] Y. Zhang, M. Ma, X. Zhang, B. Wang, R. Liu, Synthesis characterization, and catalytic property of nanosized MgO flakes with different shapes, *J. Alloys Compd.* 590 (2014) 373–379.

[67] H.R. Mahmoud, S.A. El-Moll, M. Saif, Improvement of physicochemical properties of  $\text{Fe}_2\text{O}_3$ /MgO nanomaterials by hydrothermal treatment for dye removal from industrial wastewater, *Powder Technol.* 249 (2013) 225–233.

[68] F. Parmaliana, F. Arena, N. Frusteri, Temperature-programmed reduction study of NiO–MgO interactions in magnesia-supported Ni catalysts and NiO–MgO physical mixture, *J. Chem. Soc. Faraday Trans.* 86 (1990) 2663–2669.

[69] M. Usman, W.M.A.W. Daud, An investigation on the influence of catalyst composition, calcination and reduction temperatures on Ni/MgO catalyst for dry reforming of methane, *RSC Adv.* 6 (2016) 91603–91616.

[70] G.T. Wurzler, R.C.R. Neto, L.V. Mattos, M.A. Fraga, F.B. Noronha, Steam reforming of ethanol for hydrogen production over MgO-supported Ni-based catalysts, *Appl. Catal. A* 518 (2016) 115–128.

[71] J. Ashok, G. Raju, P.S. Reddy, M. Subrahmanyam, A. Venugopal, Catalytic decomposition of  $\text{CH}_4$  over  $\text{NiO}-\text{Al}_2\text{O}_3-\text{SiO}_2$  catalysts: influence of catalyst preparation conditions on the production of  $\text{H}_2$ , *Int. J. Hydrogen Energy* 33 (2008) 4809–4818.

[72] Y.H. Hu, E. Ruckenstein, Binary MgO-based solid solution catalysts for methane conversion to syngas, *Catal. Rev. Sci. Eng.* 44 (2002) 423–453.

[73] W. Gac, A. Denis, T. Borowiecki, L. Kepinski, Methane decomposition over Ni–MgO–Al<sub>2</sub>O<sub>3</sub> catalysts, *Appl. Catal. A: Gen.* 357 (2009) 236–243.

[74] X. Li, D. Li, H. Tian, L. Zeng, Z.J. Zhao, J. Gong, Dry reforming of methane over  $\text{Ni}/\text{La}_2\text{O}_3$  nanorod catalysts with stabilized Ni nanoparticles, *Appl. Catal. B* 202 (2017) 683–694.

[75] D. Kang, J.W. Lee, Enhanced methane decomposition over nickel–carbon–B<sub>2</sub>O<sub>3</sub> core–shell catalysts derived from carbon dioxide, *Appl. Catal. B* 186 (2016) 41–55.

[76] L. Tang, D. Yamaguchi, N. Burke, D. Trimm, K. Chiang, Methane decomposition over ceria modified iron catalysts, *Catal. Commun.* 11 (2010) 1215–1219.

[77] N. Bayat, M. Rezaei, F. Meshkani, Methane dissociation to CO<sub>x</sub>-free hydrogen and carbon nanofiber over Ni-Cu/Al<sub>2</sub>O<sub>3</sub> catalysts, *Fuel* 195 (2017) 88–96.

[78] H.Y. Wang, A.C. Lua, Methane decomposition using Ni-Cu alloy nano-particle catalysts and catalyst deactivation studies, *Chem. Eng. J.* 262 (2015) 1077–1089.

[79] G. Naresh, V. Vijay Kumar, C. Anjaneyulu, J. Tardio, S.K. Bhargava, J. Patel, A. Venugopal, Nano size H $\beta$  zeolite as an effective support for Ni and Ni-Cu for CO<sub>x</sub> free hydrogen production by catalytic decomposition of methane, *Int. J. Hydrogen Energy* 41 (2016) 19855–19862.

[80] A.H. Al-Fatesh, A.A. Fakieha, W.U. Ibrahim, H. Khan, R. Atia, K. Eckelt, B. Seshan, Decomposition of methane over alumina supported Fe and Ni-Fe bimetallic catalyst: effect of preparation procedure and calcination temperature, *J. Saudi Chem. Soc.* (2016), <http://dx.doi.org/10.1016/j.jscs.2016.05.001>.

[81] Y. Shen, A.C. Lua, Sol-gel synthesis of titanium oxide supported nickel catalysts for hydrogen and carbon production by methane decomposition, *J. Power Sources* 280 (2015) 467–475.

[82] A.E. Awadallah, D.S. El-Desouki, N.A.K. Aboul-Gheit, A.H. Ibrahim, A.K. Aboul-Gheit, Effect of crystalline structure and pore geometry of silica based supported materials on the catalytic behavior of metallic nickel particles during methane decomposition to CO<sub>x</sub>-free hydrogen and carbon nanomaterials, *Int. J. Hydrogen Energy* 41 (2016) 16890–16902.

[83] A.H. Fakieha, A.A. Ibrahim, M.A. Naem, W.U. Khan, A.E. Abasaeed, R.L. Alotaibi, A.S. Al-Fatesh, Methane decomposition over Fe supported catalysts for hydrogen and nano carbon yield, *Catal. Sustain. Energy* 2 (2015) 71–82.

[84] A.A. Ibrahim, A.H. Fakieha, A.S. Al-Fatesh, A.E. Abasaeed, W.U. Khan, Methane decomposition over iron catalyst for hydrogen production, *Int. J. Hydrogen Energy* 40 (2015) 7593–7600.

[85] A.E. Ahmed, A.A. Awadallah, Ni/CeO<sub>2</sub>–Al<sub>2</sub>O<sub>3</sub> catalysts for methane thermo-catalytic decomposition to CO<sub>x</sub>-free H<sub>2</sub> production, *Int. J. Hydrogen Energy* 41 (2016) 18484–18493.

[86] L. Zhou, L.R. Enakonda, M. Harb, A. Aguilar-Tapia Y. Saib, S. Ould-Chikh, J. Hazemann, J. Li, N. Wei, D. Gary, P. Del-Gallo, Fe catalysts for methane decomposition to produce hydrogen and carbon nano materials, *Appl. Catal. B* 208 (2017) 44–59.

[87] A.E. Awadallah, A.A. Aboul-Enein, A.K. Aboul-Gheit, Various nickel doping in commercial Ni-Mo/Al<sub>2</sub>O<sub>3</sub> as catalysts for natural gas decomposition to CO<sub>x</sub>-free hydrogen production, *Renew. Energy* 57 (2013) 671–678.

[88] Y. Echegoyen, I. Suelves, M.J. Lazaro, M.L. Sanjuán, R. Moliner, Thermo catalytic decomposition of methane over Ni-Mg and Ni-Cu-Mg catalysts: effect of catalyst preparation method, *Appl. Catal. A* 333 (2007) 229–237.

[89] M. Pudukudy, Z. Yaakob, M.S. Takriff, Methane decomposition over Pd promoted Ni/MgAl<sub>2</sub>O<sub>4</sub> catalysts for the production of CO<sub>x</sub> free hydrogen and multiwalled carbon nanotubes, *Appl. Surf. Sci.* 356 (2015) 1320–1326.

[90] J.L. Pinilla, I. Suelves, M.J. Lazaro, R. Moliner, J.M. Palacios, Parametric study of the decomposition of methane using a NiCu/Al<sub>2</sub>O<sub>3</sub> catalyst in a fluidized bed reactor, *Int. J. Hydrogen Energy* 35 (2010) 9801–9809.

[91] R. Utrilla, J.L. Pinilla, I. Suelves, M.J. Lázaro, R. Moliner, Catalytic decomposition of methane for the simultaneous co-production of CO<sub>2</sub>-free hydrogen and carbon nanofibre based polymers, *Fuel* 90 (2011) 430–432.

[92] L. Ni, K. Kuroda, L.P. Zhou, K. Ohta, K. Matsuishi, J. Nakamura, Decomposition of metal carbides as an elementary step of carbon nanotube synthesis, *Carbon* 47 (2009) 3054–3062.

[93] L.R. Enakonda, L. Zhou, Y. Saib, S. Ould-Chikh, S. Lopatin, D. Gary, P. Del-Gallo, J.-M. Basset, Methane-induced activation mechanism of fused ferric oxide-alumina catalysts during methane decomposition, *Chem. Sus. Chem.* 9 (2016) 1911–1915, <http://dx.doi.org/10.1002/cssc.201600500>.

[94] M. Hasebe, H. Ohtani, T. Nishizawa, Effect of magnetic transition on solubility of carbon in bcc Fe and fcc Co-Ni alloys, *Metall. Trans. A* 16 (1985) 913–921.

[95] C.T. Wirth, B.C. Bayer, A.D. Gamalski, S. Esconjauregui, R.S. Weatherup, C. Ducati, C. Baetz, J. Robertson, S. Hofmann, The phase of iron catalyst nanoparticles during carbon nanotube growth, *Chem. Mater.* 24 (2012) 4633–4640.

[96] R.J. Wrobel, A. Helminiaik, W. Arabczyk, U. Narkiewicz, Studies on the kinetics of carbon deposit formation on nanocrystalline iron stabilized with structural promoters, *J. Phys. Chem. C* 118 (2014) 15434–15439.

[97] R. Sharma, E. Moore, P. Rez, M.M.J. Treacy, Site-Specific fabrication of Fe particles for carbon nanotube growth, *Nano Lett.* 9 (2009) 689–694.

[98] Y. Shen, A.C. Lua, A facile method for the large-scale continuous synthesis of graphene sheets using a novel catalyst, *Sci. Rep.* 3 (2013), <http://dx.doi.org/10.1038/srep03037>, Article number: 3037.

[99] P. Jana, V.A. de la, P. O'Shea, J.M. Coronado, D.P. Serrano, Co-production of graphene sheets and hydrogen by decomposition of methane using cobalt based catalysts, *Energy Environ. Sci.* 4 (2011) 778–783.

[100] A.E. Awadallah, A.A. Aboul-Enein, U.F. Kandil, M.R. Taha, Facile and large-scale synthesis of high quality few-layered graphene nano-platelets via methane decomposition over unsupported iron family catalysts, *Mater. Chem. Phys.* 191 (2017) 75–85.

[101] M. Pudukudy, A. Kadier, Z. Yaakob, M.S. Takriff, Non-oxidative thermocatalytic decomposition of methane into CO<sub>x</sub> free hydrogen and nanocarbon over unsupported porous NiO and Fe<sub>2</sub>O<sub>3</sub> catalysts, *Int. J. Hydrogen Energy* 41 (2016) 18509–18521.

[102] M. Pudukudy, Z. Yaakob, N. Dahan, M.S. Takriff, N.S.M. Hassan, Production of CO<sub>x</sub> free hydrogen and nanocarbon via methane decomposition over unsupported porous nickel and iron catalysts, *J. Clust. Sci.* 28 (2017) 1579–1594, <http://dx.doi.org/10.1007/s10876-017-1173-5>.

[103] G.B. Nuernberg, E.L. Foletto, L.F.D. Probst, N.L.V. Carreno, M.A. Moreira, MgAl<sub>2</sub>O<sub>4</sub> spinel particles prepared by metal-chitosan complexation route and used as catalyst support for direct decomposition of methane, *J. Mol. Catal. A: Chem.* 370 (2013) 22–27.

[104] Y. Kameya, K. Hanamura, Kinetic and Raman spectroscopic study on catalytic characteristics of carbon blacks in methane decomposition, *Chem. Eng. J.* 173 (2011) 627–635.

[105] L. Dong, Y. Du, J. Li, H. Wang, Y. Yang, et al., The effect of CH<sub>4</sub> decomposition temperature on the property of deposited carbon over Ni/SiO<sub>2</sub> catalyst, *Int. J. Hydrogen Energy* 40 (2015) 9670–9676.

[106] P. Lespade, A. Marchand, M. Couzi, F. Crouzet, Caracterisation de matériaux carbones par microspectrométrie Raman, *Carbon* 22 (1984) 375–385.

[107] I. Childres, L.A. Jauregui, W. Park, H. Cao, Y.P. Chen, Raman spectroscopy of graphene and related materials, [https://www.physics.psu.edu/quantum/files/Raman\\_Spectroscopy\\_of.Graphene\\_NOVA.Childres.pdf](https://www.physics.psu.edu/quantum/files/Raman_Spectroscopy_of.Graphene_NOVA.Childres.pdf).